



Integration of metal organic framework nanoparticles into sodium alginate biopolymer-based three-dimensional membrane capsules for the efficient removal of toxic metal cations from water and real sewage

Imran Ali ^{a,b,c,1}, Peng Wan ^{d,e,1}, Changsheng Peng ^f, Xiao Tan ^c, Huibin Sun ^b, Juying Li ^{a,*}

^a Department of Environmental Engineering, College of Chemistry and Environmental Engineering, Shenzhen University, Shenzhen 518060, China

^b Key Laboratory of Optoelectronic Devices and Systems, College of Physics and Optoelectronic Engineering, Ministry of Education and Guangdong Province, Shenzhen University, Shenzhen, 518060, China

^c College of Environment, Hohai University, Nanjing, Jiangsu, 210024, China

^d Shenzhen Water Planning & Design Institute Co., Ltd., Shenzhen 518001, China

^e Guangdong Provincial Engineering and Technology Research Center for Water Affairs Big Data and Water Ecology, Shenzhen, 518001, China

^f School of Chemical and Environmental Engineering, Anhui Polytechnic University, Wuhu 241000, China



ARTICLE INFO

Keywords:

Sodium alginate biopolymer
Metal organic framework nanoparticles
Membrane capsules
Toxic metals cations
Adsorption mechanism
Real sewage

ABSTRACT

Sodium alginate (SA) biopolymer has been recognized as an efficient adsorbent material owing to their unique characteristics, including biodegradability, non-toxic nature, and presence of abundant hydrophilic functional groups. Accordingly, in the current research work, UiO-66-OH and UiO-66-(OH)₂ metal organic framework (MOF) nanoparticles (NPs) have been integrated into SA biopolymer-based three-dimensional (3-D) membrane capsules (MCs) via a simple and facile approach to remove toxic metal cations (Cu^{2+} and Cd^{2+}) from water and real sewage. The newly configured capsules were characterized by FTIR, SEM, XRD, EDX and XPS analyses techniques. Exceptional sorption properties of the as-developed capsules were ensured by evaluation of the pertinent operational parameters, i.e., contents of MOF-NPs (1–100 wt%), adsorbent dosage (0.001–0.05 g), contact time (0–360 h), pH (1–8), initial concentration of metal cations (5–1000 mg/L) and reaction temperature (298.15–333.15 K) on the eradication of Cu^{2+} and Cd^{2+} metal cations. It was found that hydrophilic functional groups (-OH and -COOH) have performed an imperative role in the smooth loading of MOF-NPs into 3-D membrane capsules via intra/inter-molecular hydrogen bonding and van der waals potencies. The maximum monolayer uptake capacities (as calculated by the Langmuir isotherm model) of Cd^{2+} and Cu^{2+} by 3-D SGMMCs-OH were 940 and 1150 mg/g, respectively, and by 3-D SGMMCs-(OH)₂ were 1375 and 1575 mg/g, respectively, under optimum conditions. The as-developed capsules have demonstrated superior selectivity against targeted metal cations under designated pH and maintained >80 % removal efficiency up to six consecutive treatment cycles. Removal mechanisms of metal cations by the 3-D SGMMCs-OH/(OH)₂ was proposed, and electrostatic interaction, ion-exchange, inner-sphere coordination bonds/interactions, and aromatic ligands exchange were observed to be the key removal mechanisms. Notably, FTIR and XPS analysis indicated that hydroxyl groups of Zr-OH and BDC-OH/(OH)₂ aromatic linkers played vital roles in Cu^{2+} and Cd^{2+} adsorption by participating in inner-sphere coordination interactions and aromatic ligands exchange mechanisms. The as-prepared capsules indicated >70 % removal efficiency of Cu^{2+} from real electroplating wastewater in the manifestation of other competitive metal ions and pollutants under selected experimental conditions. Thus, it was observed that newly configured 3-D SGMMCs-OH/(OH)₂ have offered a valuable discernment into the development of MOFs-based water decontamination 3-D capsules for industrial applications.

* Correspondence to: J. Li, College of Chemistry and Environmental Engineering, Shenzhen University, Shenzhen 518060, China

E-mail addresses: enrgimran56@gmail.com (I. Ali), jyli@szu.edu.cn (J. Li).

¹ These authors contributed equally to this work.

1. Introduction

Potentially toxic metals (PTMs), such as Pb^{2+} , Cu^{2+} , Hg^{2+} , Cd^{2+} , Ni^{2+} , Zn^{2+} , Mg^{2+} , Cr^{3+} and Cr(VI) are considered as the main contaminants in industrial effluents, which commence a significant menace to biotic and aquatic life due to their carcinogenicity, teratogenicity and mutagenicity behavior [1–5]. PTMs are arduous to degrade into environment friendly constituents, it bioaccumulate in biological tissue, and can initiate various kinds of diseases in humans including kidney disorders, lung infection, abdominal pain, genetic disorders, choking and ulcer formation [6–8]. Several industries including metal finishing, painting, lead smelters, ceramics, electroplating, petroleum refineries, battery manufacturing and pigment, are discharging a huge amount of untreated PTMs-contaminated sewage into the natural water bodies [9,10]. Therefore, the decontamination of PTMs is of vital prominence for both public and environmental health.

Over the past few years, various methods such as filtration, solvent extraction, oxidation, chemical precipitation, adsorption, biological treatments, photocatalysis, evaporative recovery, reverse osmosis, electrocoagulation and membrane technologies have been employed to eradicate PTMs from wastewater [11–17]. However, certain drawbacks, i.e., low elimination performance, generation of large amounts of toxic sludge/un-wanted by-products, higher capital investment, etc., have halted its commercial implantations. However, as compared to these technologies, adsorption is a reliable, effective, simple and cost-effective to capture and recover PTMs from wastewaters [18,19]. Several kinds of sorbents comprising clay minerals, agronomic waste, industrial by-products, layered double hydroxides, active carbon, organic resins, nanoparticles, and carbon nanotubes have been employed to eradicate PTMs. Though, these sorbents have one or several of the following hitches: (i) lower sorption performance; (ii) poor selectivity; (iii) lower stability and mechanical properties; (iv) complicated synthesis protocols; (v) lower production scale; (vi) low frequency of reusability and (vii) extremely small pore sizes and surface area of volumes ratio [20,21]. To combat these issues, the development of advanced materials is substantially needed with highly economic protocols, an excellent eradication performance and recycling ability.

Presently, metal-organic frameworks (MOFs) are being widely utilized to eradicate and recover PTMs from water environment. MOFs-type materials have depicted superior porosity, crystallinity, stability, controllable pore size, structural tailor-ability, surface area and diverse pendant reactive functional groups [17,22,23]. Furthermore, they have been employed in electronic devices, gas storage or separation, catalysis, drug delivery/carrier, luminescence sensing and pollutants remedy because of their exceptional stability under punitive environments [24–26]. For instance, various kinds of PTMs (As^{3+} , As^{5+} , Sb^{5+} , Pb^{2+} , Cd^{2+} , Al^{3+} , Hg^{2+} , Fe^{3+} , Li^+ , Co^{2+} , Cu^{2+} and Pt^{4+}), have been successfully removed via MOFs-type materials because they can provide a strong chelating potency between PTMs and reactive functional groups of organic linkers and tunable pores for the sorption of PTMs [27–30]. Despite having superior adsorbability against PTMs, their practical applications are limited because of the requirement of higher MOFs content. Moreover, MOFs have expensive synthesis prerequisites and have indicated difficulty in separation from the final effluents due to their extremely small particles size (5–100 nm) which tend to shape flimsy water suspensions that can either transport through the columns or consequence in column choking [31,32]. To solve these issues, recently, the incorporation of MOFs-type materials into membranes has been extensively explored for the remediation of environmental pollutants. Membrane-based technologies are famous due to their high porosity, high adsorbability, greater surface area-to-volume ratio and higher selectivity in a variety of applications including wastewater treatment and seawater desalination [33–35]. A team of research investigators, have incorporated various kinds of MOFs-type materials into different membranes due to their higher permeability and selective porosity for water filtration [36]. However, the leaching/mass loss of MOF-NPs is a

big menace for the transfer of MOF-based membrane technologies from laboratory-scale to the practical applications. To resolve this issue, an innovative and facile method was employed in the present work to incorporate UiO-66-OH and UiO-66-(OH)₂ MOF-NPs into 3-D MCs to shape powder-state MOFs to macrobody, which can avoid the mass loss of MOFs particles during the adsorption process. Thus, a green biopolymer such as alginate was blended with UiO-66-OH and UiO-66-(OH)₂ MOF-NPs to develop novel 3-D SGMMCs-OH and 3-D SGMMCs-(OH)₂ capsules because both MOF-NPs and alginate had plentiful -OH and -COOH functional groups for the smooth coordination and eradication of PTMs under designated pH. While, alginate is a polysaccharide biopolymer [37], isolated from brown, red, green, blue algae cells, and bacterial materials, which contain 30–60 % alginic acid. It has α -L-guluronic (G) with 1,4- β -D-mannuronic (M) acids in a monomer [38]. It has the effective -OH and -COOH functional groups. Alginate supported materials have been broadly utilized for the toxic ions' adsorption owed to its advantages like biocompatibility, cost-effectiveness, biofunctionality, non-toxicity, and biodegradability. However, it possesses swelling nature and low mechanical strength, which effects its adsorbability [39]. Hence, MOF-NPs were uniformly dispersed into alginate matrix to form three-dimensional (3-D) membrane capsules composite for the adsorption of toxic metal cations. Therefore, the objectives of this study were (i) to integrate UiO-66-OH and UiO-66-(OH)₂ metal organic framework nanoparticles into 3-D membrane capsules for the efficient removal of toxic metal cations (Cd^{2+} and Cu^{2+}) from water and real sewage, (ii) to investigate the underlying eradication mechanism of metal cations by 3-D SGMMCs-OH/(OH)₂, and (iii) to explore the suitability of as-developed 3-D SGMMCs-OH/(OH)₂ in real electroplating wastewater treatment. Herein, the acronyms S, G, M and MCs in the 3-D SGMMCs material represent sodium alginate, glutaraldehyde, MOF NPs, and membrane capsules, respectively.

2. Materials and methods

2.1. Chemicals, reagents, and instrumentations

The details of the chemicals, reagents and instrumentations used in the current research have been documented in the supplementary information (Text SI).

2.2. Synthesis of UiO-66-OH and UiO-66-(OH)₂-NPs

For the fabrication of UiO-66-OH-NPs, the DMF (30 mL) solution was trickled dropwise in the amalgam of 2-Hydroxyterephthalic acid $\text{C}_8\text{H}_6\text{O}_5$ (H2BDC-OH) (0.16613 g, 1 mmol) and ZrCl_4 (0.2330 g, 1 mmol). Thereafter, the acetic acid (7 mL) solution was injected into the above mixture and held under magnetic stirring for 30 min at room temperature. The obtained amalgam was shifted to a 100 mL Teflon-lined-stainless-steel autoclave and heated at 150 °C for 48 h, followed by centrifugation at 10000 rpm for 10 min. After centrifugation, the supernatant was removed, and the sediment was cleaned and immersed in methanol for 24 h. After this, the light yellowish powder was separated by centrifugation, and then dehydrated under vacuum at 60 °C for 24 h to obtain UiO-66-OH-NPs for further loading into 3-D SMCs. Similar protocol was followed to fabricate yellowish UiO-66-(OH)₂-NPs using chemical linker (i.e., 2,5-Dihydroxyterephthalic acid ($\text{HO}_2\text{C}_6\text{H}_2\text{-1,4-(CO}_2\text{H}_2$)₂) (DOBDC; H2BDC-(OH)₂) with the same prerequisites as stated above. In addition, the characteristics of chemical linkers used for the fabrication of MOFs-NPs were presented in the Table 1.

2.3. Development of novel mixed matrix 3-dimensional membrane capsules containing UiO-66-OH and UiO-66-(OH)₂ metal organic framework-nanoparticles (3-D SGMMCs-OH and 3-D SGMMCs-(OH)₂)

For the fabrication of novel mixed matrix 3-D membrane capsules (3-D MCs), a simple two-step-titration-gel crosslinking approach was

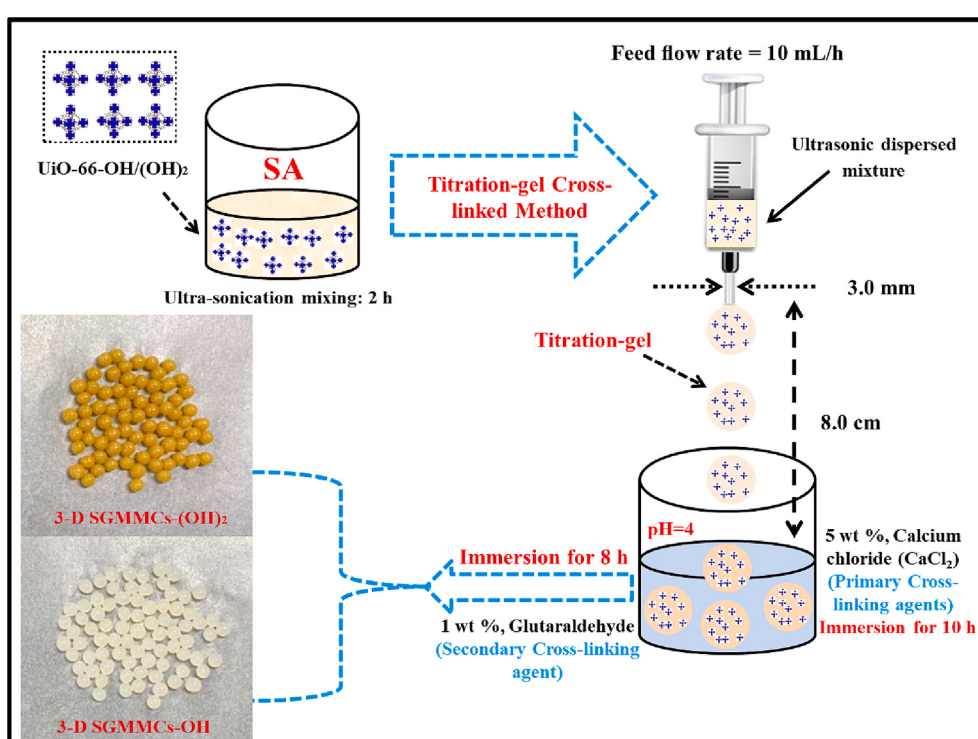
Table 1

Characteristics of chemical linkers used for the synthesis of metal-organic frameworks-nanoparticles (MOFs-NPs) and color of final MOFs-NPs.

Sr. No	MOF-NPs	Name	Chemical formula	Molecular weight	Chemical structure	Color of final MOFs-NPs
1	UiO-66-OH	2-Hydroxyterephthalic acid	C ₈ H ₆ O ₅	166.131		
2	UiO-66-(OH) ₂	2,5-Dihydroxyterephthalic acid	(HO) ₂ C ₆ H ₂ -1,4-(CO ₂ H) ₂	198.13		

followed by the crosslinking of SA-UiO-66-OH/(OH)₂ solution with CaCl₂ and GA as a primary and secondary crosslinking agent, respectively, in the manifestation of UiO-66-OH/(OH)₂ MOF-NPs. The SA emulsion (3 wt%) was crafted by dissolving 3 g SA powder into 97 g water and held at 90 °C in oven for 24 h to confirm uniform suspension and swelling. Thereafter, 70 wt% SA-UiO-66-OH and 60 % wt% SA-UiO-66-(OH)₂ solutions were prepared by blending 1.05 g UiO-66-OH-MOF-NPs and 0.90 g UiO-66-(OH)₂-MOF-NPs in 48.95 & 49.10 g SA solution, respectively, and kept under ultra-sonication missing for at-least 2 h, until a uniform suspension was achieved. Primary crosslinking emulsion CaCl₂ (5 wt%) was prepared independently by dissolving 13.58 g CaCl₂ powder in 250 mL DI water and the pH of the emulsion was maintained at 4 exploiting 0.1 mol/L NaOH and HCl. Likewise, a secondary crosslinking emulsion of GA (1 wt%) was made individually by inserting 2 mL GA solution into 98 mL of DI water. Thereafter, the ultrasonic dispersed mixture of SA-UiO-66-OH/(OH)₂ (70/60 wt%) was shifted into a nozzle that had nettle diameter about 3.0 mm, and it was situated horizontally in a nozzle injection pump by regulating feed flow rate of 10 mL/h. After this, the amalgam droplet was trickled into primary crosslinking

liquid via nozzle injection pump by upholding a gap of 8.0 cm between nettle top to primary crosslinking cocktail surface. Then, as-fabricated capsules were retained into primary crosslinking blend for at-least 24 h to develop 3-D SGMMCs-OH/(OH)₂ with a sound stiffness, ductility and robust exterior surface. Next, these capsules were smoothly isolated from primary crosslinking emulsion, and submerged into secondary crosslinking suspension, i.e., GA (1 wt%) for 8 h to enhance shape toughness and mechanistic characteristics. At this time, the as-developed 3-D SGMMCs-OH/(OH)₂ were isolated and rinsed completely six to seven times with deionized water. Finally, these capsules were preserved using freeze dryer for advance sorption experiments. The schematic of the development of 3-D SGMMCs-OH/(OH)₂ has been portrayed in the Fig. 1. In addition, various types of 3-D SGMMCs-OH/(OH)₂ were also synthesized by incorporating various amount of UiO-66-OH/(OH)₂-MOF-NPs (1 to 100 wt%/0.015 to 1.50 g) into the SA mixture for optimizing the fabrication protocol and examining the influence of UiO-66-OH/(OH)₂-MOF-NPs loading on the sorption performance (Table S1).

**Fig. 1.** Schematic illustration of the development of 3-D SGMMCs-OH/(OH)₂ by loading UiO-66-OH/(OH)₂-MOF-NPs.

2.4. Characterization of the developed 3-D SGMMCs-OH/(OH)₂

The details about characterization of the as-developed 3-D SGMMCs-OH/(OH)₂ have been described in the supplementary Information (Text SII).

2.5. Adsorption experiments

The details of all executed experiments are incorporated into the supplementary information (Text SIII). Further the following equations were employed to estimate the removal efficiency, adsorption capacity and sorption-desorption efficiencies:

$$\text{Removal efficiency (\%)} = \frac{C_o - C_t}{C_o} \times 100\% \quad (1)$$

$$\text{Adsorption amount, } q_e(\text{mg/g}) = \frac{(C_o - C_e) * V}{M} \quad (2)$$

$$\text{Desorption efficiency, } \eta(\%) = \frac{M_{\text{desorbed}}}{M_{\text{sorbed}}} \times 100\% = \frac{(C_r \times V_r)}{(C_o - C_e) \times V} \times 100\% \quad (3)$$

where, the C_o (mg/L) and C_t (mg/L) are the initial and final PTMs concentration at zero and time t , respectively. The C_e (mg/L) is the concentration of PTMs at time equilibrium. M (g) is the amount of 3-D SGMMCs, and V (L) is the volume of PTMs solution. In addition, M_{desorbed} and M_{sorbed} are the quantity of metals adsorbed and desorbed from the 3-D SGMMCs. V (L) and V_r (L) is the volume of feed and regeneration solution, respectively.

2.6. Practical application of 3-D SGMMCs-OH/(OH)₂ in real electroplating wastewater

The practicability of the as-developed 3-D SGMMCs was explored using real electroplating wastewaters. The real electroplating wastewaters were collected from four different industries, located at Shenzhen city, China (herein named as A, B, C and D, respectively). To explore the functionality of 3-D SGMMCs-OH/(OH)₂ to eradicate targeted cationic metal ions, copper-containing real electroplating wastewaters were particularly collected before its mixing with other processing steps discharges. The samples were collected in clean plastic bottles, filtered, and then analyzed in the laboratory according to standard methods. The physico-chemical characterization of the collected sewage samples is presented in Table SII. The pH of copper-containing real electroplating wastewaters was initially adjusted at 6. Thereafter, two different dosages (1 g and 1.5 g) of sorbents were added into 50 mL of the sewage samples, and shaken at 130 rpm for five days, and temperature of the shaker was adjusted at 298.15 K. The concentrations/values of PTMs and other pertinent parameters were estimated after filtering samples using 0.22 µm Syringe filter. Finally, the debate was made by comparing removal efficiencies of real electroplating wastewaters with single Cu-

containing synthetic wastewater for better understanding the practicability of as-developed 3D SGMMCs-OH/(OH)₂.

3. Result and discussion

3.1. Characterization of the As-developed 3-D SGMMCs-OH/(OH)₂

3.1.1. Physical properties

Table 2 depicts the physical properties of the as-synthesized 3-D SGMMCs-OH/(OH)₂. The values of aspect ratio indicated that the developed SGMMCs-OH/(OH)₂ were near to an ideal sphere. The values of swelling ratio/water content revealed that the 3-D SGMMCs-OH and 3-D SGMMCs-(OH)₂ could seize approximately 95.55 % and 96.55 % water content, respectively, because of the presence of plentiful hydrophilic functional groups. Moreover, the mean diameter of the as-fabricated 3-D SGMMCs-OH/(OH)₂ was 3 ± 0.02 mm.

3.1.2. The formation principle of the 3-D SGMMCs-OH/(OH)₂

The FTIR spectra of SA, MOF-NPs, 3-D SMCs, 3-D SGMMCs-OH and 3-D SGMMCs-(OH)₂ were explored to understand the formation principle of the as-developed capsules, such as the role of hydrophilic groups in the smooth loading of MOF-NPs in/on the membrane capsule (MC) (Fig. 2(I-II)). These findings depicted that the strips at 3600–3300 cm⁻¹ can be endorsed to O—H stretching vibrational alps of polyphenolic groups and the stripes at 3202–2909 cm⁻¹ can be ascribed to —C—H stretching vibrational peaks of alkanes. The peaks at round 1560–1375 cm⁻¹ can be allocated to C—OH stretching/-COO⁻ groups of SA. Moreover, the peaks emerged at 1640 and 892 cm⁻¹ were clearly proving C=O stretching and the manifestation of O—Na bonds in —COONa radical of SA, respectively. Similarly, the FTIR spectrum of UiO-66-OH and UiO-66-(OH)₂ MOF-NPs were also studied and the findings revealed a broad peak in the range of 3670–3350 cm⁻¹, which can be allocated to O—H stretching vibrational alps of polyphenolic groups [40]. The stripes at 3200–2900 cm⁻¹ can be ascribed to —C—H stretching vibrational peaks of alkanes. The Zr—O stretching peaks at approximately 805 cm⁻¹ and 680 cm⁻¹ originated from the Zr metal clusters, and these peaks were clearly indicating the presence of Zr—O bond/Zr (μ_3 O) of UiO-66-OH and UiO-66-(OH)₂ MOF structure, respectively [41–43]. Notably, the absorption bands at 1205–1386 cm⁻¹ and 1201–1234 cm⁻¹ can be corresponded to the C—O stretching of the —OH groups from the aromatic ligands BDC-OH and BDC-(OH)₂ of UiO-66-OH and UiO-66-(OH)₂ MOF-NPs, respectively [44,45]. Further, the peaks at around 1560–1430 cm⁻¹ represented the symmetric and asymmetric stretching peaks of —C=O—O groups formed by coordination between the Zr metal center and the organic ligands BDC-OH and BDC-(OH)₂ of UiO-66-OH and UiO-66-(OH)₂ MOF-NPs, respectively [46]. Notably, the peaks at around 1640 cm⁻¹ and 1592 cm⁻¹ in the FTIR spectra of UiO-66-OH and UiO-66-(OH)₂ MOF-NPs can be corresponded to the presence of free carboxyl functional groups (COOH), monodentate COO⁻ ligands, and/or C=C vibration of the benzene ring [24,47,48]. The characteristic

Table 2
Physical properties of the as-prepared 3-D SGMMCs-OH/(OH)₂.

Parameters	Instrument used/equation	Unit	Values	
			3-D SGMMCs-OH	3-D SGMMCs-(OH) ₂
Average wet weight/capsule	Weight balance	g	0.0280 ± 0.001	0.0285 ± 0.001
Average freeze-dried weight/capsule	Weight balance	g	0.0011 ± 0.0001	0.0013 ± 0.0001
Average maximum diameter	SEM	mm	3 ± 0.02	3 ± 0.02
Average minimum diameter	SEM	mm	2.95 ± 0.01	2.96 ± 0.01
Average density (on wet basis)	$\text{Density, } P \left(\frac{\text{g}}{\text{m}^3} \right) = \frac{M}{V}$	g/m ³	$198,159,912 \pm 0.05$	$2,016,985.14 \pm 0.05$
Average density (on dry basis)	$\text{Volume, } V \left(\text{m}^3 \right) = \frac{4\pi r^3}{3}$	g/m ³	$77,848.54 \pm 0.05$	$92,002.83 \pm 0.05$
Aspect ratio (on average)	$\text{Aspect ratio} = \frac{D_{\max}}{D_{\min}}$	(—)	1.002 ± 0.03	1.003 ± 0.03
Average water content	$\text{Water content/Swelling ratio (\%)} = \frac{(W - D)}{W} \times 100\%$	(%)	95.55 ± 0.05	96.55 ± 0.05

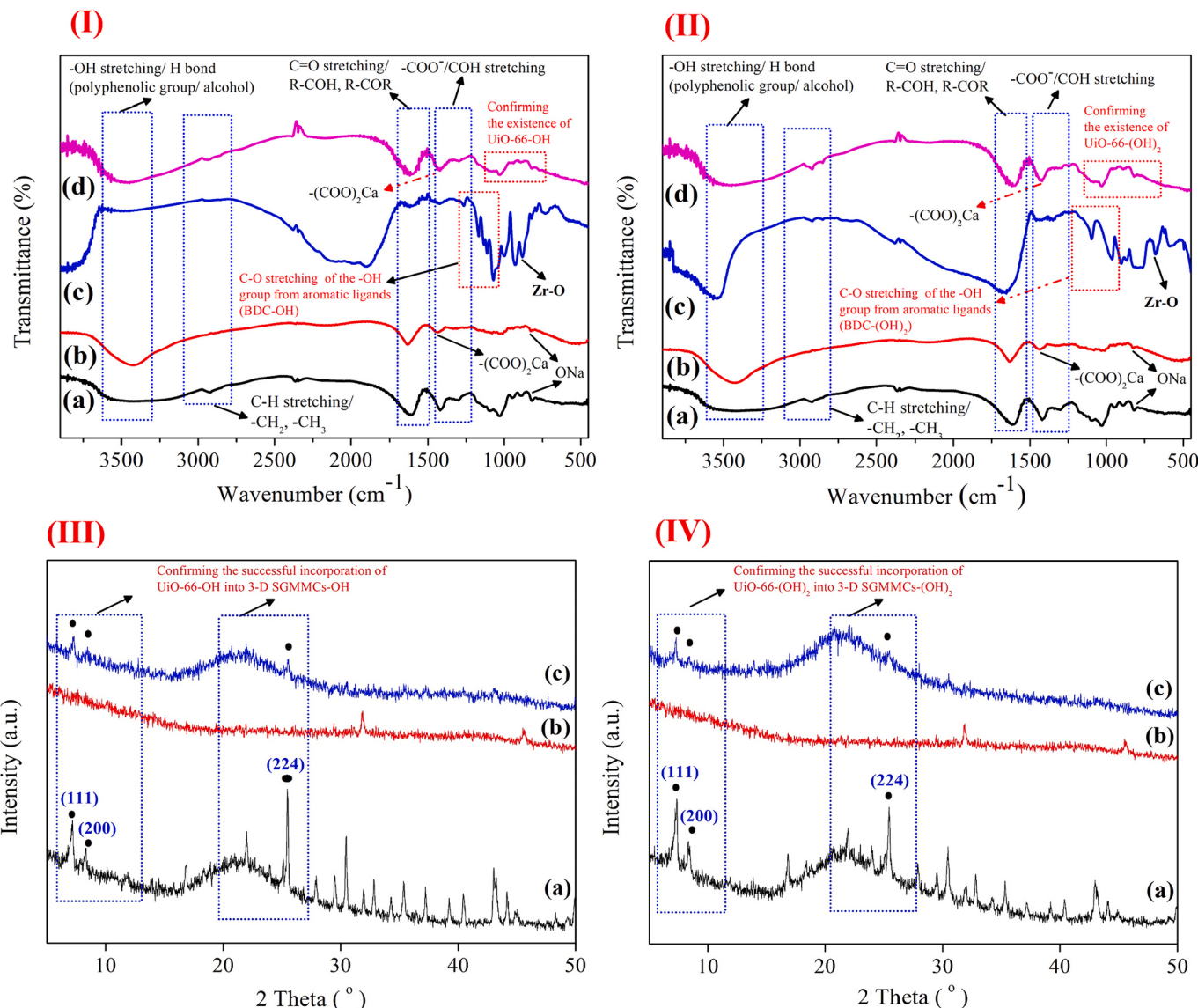


Fig. 2. (I) FTIR spectra of (a) SA, (b) 3-D SMCs, (c) UiO-66-OH and (d) 3-D SGMMCs-OH; (II) FTIR spectra of (a) S3A, (b) 3-D SMCs, (c) UiO-66-(OH)₂ and (d) 3-D SGMMCs-(OH)₂; (III) Powder XRD spectra of (a) UiO-66-OH, (b) 3-D SMCs, and (c) 3-D SGMMCs-OH; and (IV) Powder XRD spectra of (a) UiO-66-(OH)₂, (b) 3-D SMCs, and (c) 3-D SGMMCs-(OH)₂.

absorption peaks at 745 cm^{-1} and 683 cm^{-1} in the FTIR spectra of UiO-66-OH and UiO-66-(OH)₂ MOF-NPs, respectively, can be associated to the C—H out-of-plane bending of the benzene ring [49,50]. For comprehending crosslinking mechanisms, the FTIR spectra of 3-D SMCs, 3-D SGMMCs-OH and 3-D SGMMCs-(OH)₂ were also investigated. The findings portrayed that the crosslinking reaction occurred immediately by molding a liquid drop of SA-UiO-66-OH and SA-UiO-66-(OH)₂ mixtures into primary crosslinking agent/CaCl₂ solution. Thereafter, a semi-interpenetrating polymer network (SIPN) structure was primarily developed owing to the crosslinking of G units (in SA chains) with the Ca²⁺ cations via chelation, electrostatic interactions, and hydrogen bonding in the presence of UiO-66-OH and UiO-66-(OH)₂ MOF-NPs. This can be described that an ionic binding was established between Ca²⁺ and carboxyl/-COOH groups of SA, and a paltry covalent attachment was appeared between Ca²⁺ and oxygen atom (O) of ether groups, respectively. Moreover, another interaction occurred due to the bonding of -OH (of MOF-NPs) and -OH and -COH groups (of SA and GA) via hydrogen bonding and van der Waals forces. In addition, the multiple defect sites and active reactive groups on MOF-NPs can promote a stronger attachment between MOF-NPs and SA and GA via hydrogen

bonding and van der Waals forces [44]. Noticeably, the intensity of the characteristic's peaks of —OH, —COH, Zr—O, —C=O—O groups formed by coordination between the Zr metal center and the organic ligands BDC-OH and BDC-(OH)₂ of UiO-66-OH and UiO-66-(OH)₂ MOF-NPs, were also dropped after the loading of MOF-NPs, suggesting the establishment of crosslinking connections via hydrogen bonding and van der Waals forces. Further, the manifestation of Zr—O stretching peaks at around 805 cm^{-1} and 680 cm^{-1} in the FTIR spectra of UiO-66-OH and UiO-66-(OH)₂, respectively, implicit the smooth incorporation of MOF-NPs into MCs. Moreover, during secondary crosslinking with GA, the SIPN structure of SA adhered with GA exclusively, and an interpenetrating polymer network (IPN) structure was formed by crosslinking of COH groups of GA with —OH groups in SA via hydrogen bonding and van der Walls forces by escalating characteristic peaks of C=O and C—O—C stretching vibrations at around 1675 and 1085 cm^{-1} , which promoted a physical predicament and chemically crosslinked polymer network in MCs. Thus, GA operated as a 'knot' or 'joint' to tie SA and MOF-NPs together via co-crosslinking reaction that ratified inclusive mechanistic strength of MC and formulated them for more constructive sorption activity. For comprehending, the crosslinking

mechanism of MOF-NPs with the membrane capsules, pH study was designed, and the findings depicted that MOF-NPs were mainly cross-linked with the hydroxyl/-OH groups of SA, and -COH groups of GA via hydrogen bonding, and the leaching of loaded MOF-NPs was also noticed at higher pH >10 due to the breakage/destabilization of the hydrogen bonding between —OH (of MOFs-NPs) and —OH & COH groups of SA and GA, respectively. Notably, most of the MOF-NPs were smoothly crosslinked in/on the membrane capsules via hydrogen bonding even by increasing solution pH (>10), which clearly demonstrated the smooth loading of MOF-NPs and superior stability of capsules to utilize them for wide pH range (Fig. S1).

Furthermore, the powder XRD patterns of UiO-66-OH, UiO-66-(OH)₂, 3-D SMCs, 3-D SGMMCs-OH and 3-D SGMMCs-(OH)₂ were also examined (Fig. 2(III-IV) and (Fig. S2(I-II)). The heaviest characteristics peaks of UiO-66-OH and UiO-66-(OH)₂ were observed at around 2θ = 7.4°, 8.5° and 25.8°, which corresponded to (111), (200) and (224) crystal planes, respectively. These characteristic peaks of UiO-66-OH and UiO-66-(OH)₂ confirmed an excellent crystallinity and mechanical stability of the fabricated MOF-NPs [51,52]. Meanwhile, the

characteristic peaks position of UiO-66-OH and UiO-66-(OH)₂ matched well with the previous published reports [24,40–42,53,54]. The average particle diameter/crystallite size measurements of the UiO-66-OH and UiO-66-(OH)₂ MOF-NPs were also investigated by exploiting Debye–Scherrer equation and it was assessed to be about 50–60 and 150–300 nm, respectively, that was also confirmed by dynamic light scattering (DLS) technique (Fig. S2(III–IV)). Moreover, the XRD patterns of 3-D SMCs, 3-D SGMMCs-OH and 3-D SGMMCs-(OH)₂ clearly hinted the successful loading/incorporation of MOF-NPs in/on the MCs, and the titration-gel method did not significantly alter the crystallinity structure of UiO-66-OH and UiO-66-(OH)₂ MOF-NPs. The presence of diffraction peaks at around 2θ = 7.4°, 8.5° and 25.8°, which correspond to (111), (200) and (224) crystal planes, respectively, hinted the smooth incorporation of MOF-NPs in/on the MCs (Fig. S2(I–II)). However, the slightly wider peaks (of UiO-66-OH and UiO-66-(OH)₂ MOF-NPs) were witnessed and the gradual reduction of crystallinity as compared with the characteristics peaks of pure MOFs-NPs owing to the diminution of hydrophilic functional groups during the development process [55].

The EDX spectrums of UiO-66-OH, UiO-66-(OH)₂ MOF-NPs, 3-D

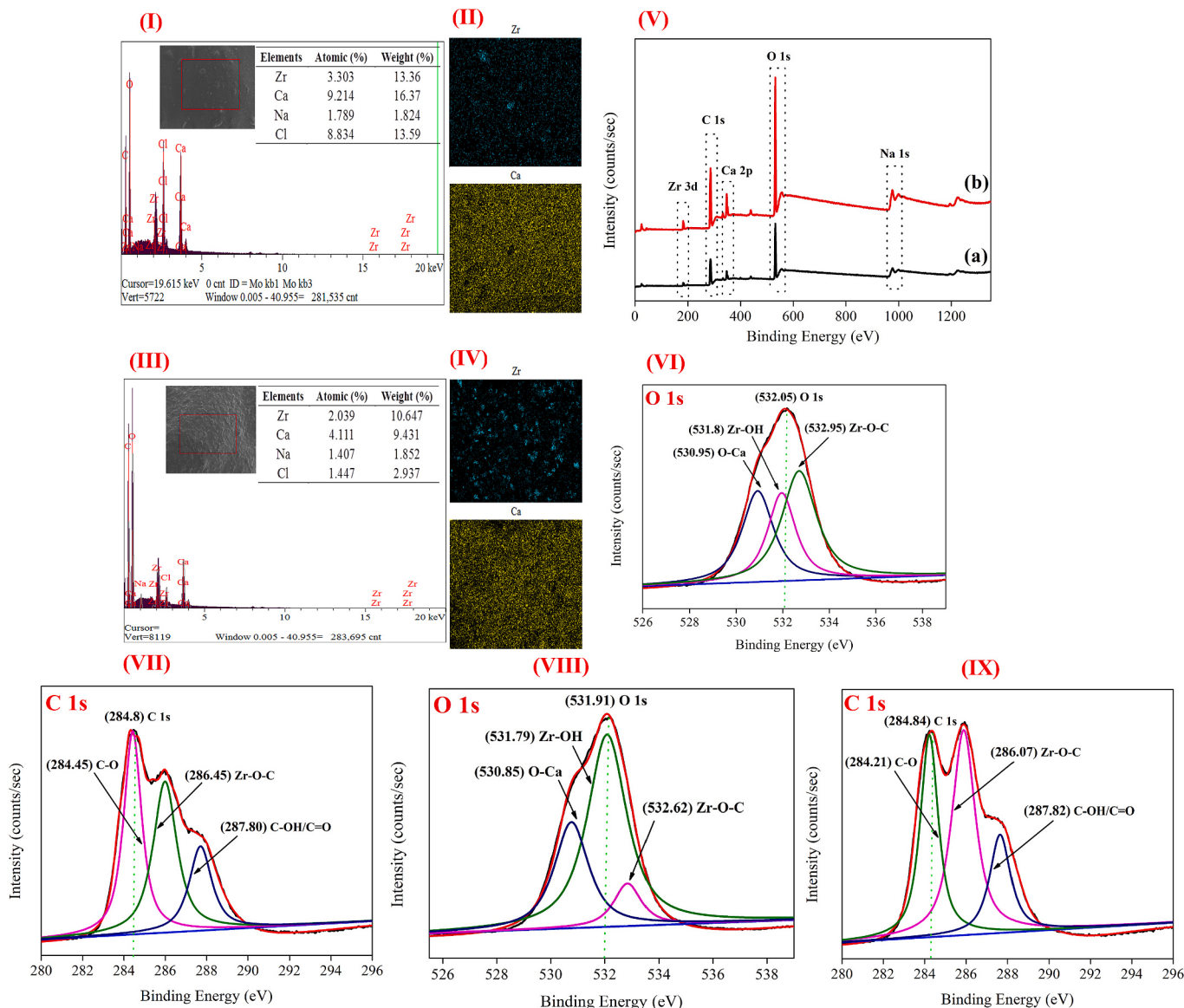


Fig. 3. (I) & (II) EDS/X mapping of 3-D SGMMCs-OH; (III) & (IV) EDS/X mapping of 3-D SGMMCs-(OH)₂; (V) X-ray photoelectron spectra (XPS) of (a) 3-D SGMMCs-OH and (b) 3-D SGMMCs-(OH)₂; high resolution XPS spectra (VI) O 1s; and (VII) C 1s of 3-D SGMMCs-OH; high resolution XPS spectra (VIII) O 1s; and (IX) C 1s of 3-D SGMMCs-(OH)₂.

SGMMCs-OH and 3-D SGMMCs-(OH)₂ were analyzed to recognize the elemental composition, and the existence of MOFs-NPs in the as-developed capsules (Fig. S3 & Fig. 3(I-IV)). The EDX spectrums comprehended strong peaks of Zr, Ca, Na and Cl (Fig. 3(I-IV)). The atomic percentages as attained by the EDX quantification (for 3-D SGMMCs-OH) were Ca (9.21 %), Zr (3.303 %), Na (1.789) and Cl (8.834 %) (Fig. 3(I-II)). Likewise, the atomic percentages as attained by the EDX quantification (for 3-D SGMMCs-(OH)₂) were Ca (4.11 %), Zr (2.039 %), Na (1.407) and Cl (1.447 %) (Fig. 3(III-IV)). The EDX spectrum comprehended strong peaks of C and O in addition to Zr, Ca, Na and Cl. The alps of C and O in EDX spectrum can be correlated with the hydrophilic functional groups (-OH and -COOH), predominantly connected with the SA, GA, and MOFs-NPs. Moreover, the incidence of Zr alp in the EDX profile endorsed the smooth loading/incorporation of MOF-NPs in/on the capsules. Also, the EDX spectrums of UiO-66-OH and UiO-66-(OH)₂ MOF-NPs were also studied and coincided with the EDX profile of 3-D SGMMCs-OH and 3-D SGMMCs-(OH)₂, which also confirmed the smooth loading of MOF-NPs in/on the capsules (Fig. S3(I-IV)). The peak of Ca can be linked with the primary crosslinking agent such as CaCl₂, though the extreme apex of Na was principally connected to SA.

The manifestation of Zr dispersed equally all over the sample, proven the uniform incorporation of MOF-NPs in the as-prepared capsules, while in a small quantity. In addition, the quantities of actual amount of MOF-NPs in the capsules were also determined using equation [56], as mentioned in the supplementary information (Text-SII), and the Zr contents in the as-developed capsules were taken from EDX/S findings [57]. The results indicated that 24.58 wt% and 21.88 wt% were the MOF-NPs load ratio in the 3-D SGMMCs-OH and 3-D SGMMCs-(OH)₂, respectively. This also confirmed the complexation between MOF-NPs and cross-linked polymer components.

Moreover, the XPS technique was also utilized to understand the formation principle of 3-D SGMMCs-OH/(OH)₂ and the attachment of MOF-NPs in the capsules. The XPS spectrum of 3-D SGMMCs-OH revealed the main signal peaks at around 284.8, 532.05, 347.02, 182.19, and 1071.03 eV harmonizing to the elements of C 1s, O 1s, Ca 2p, Zr 3d, and Na 1s, respectively (Fig. 3(Va)). Likewise, the XPS spectrum of 3-D SGMMCs-(OH)₂ revealed the main signal peaks at around 284.84, 531.91, 346.84, 182.03, and 1071.05 eV conforming to the elements of C 1s, O 1s, Ca 2p, Zr 3d, and Na 1s, respectively (Fig. 3(Vb)). Moreover, to verify the key functional groups of the materials, the high resolution XPS spectra of O 1s, C 1s and Zr 3d of 3-D SGMMCs-OH/(OH)₂ were also explored. In case of 3-D SGMMCs-OH, the peaks at around 532.95, 531.80 and 530.95 eV were corresponded to Zr-O-C, Zr-OH and O-Ca, respectively (Fig. 3(VI)). The alps at nearby 284.45, 286.45 and 287.80 eV were resembled to C—O, Zr—O—C and C—OH/C=O, respectively (Fig. 3(VII)). Further, in case of 3-D SGMMCs-(OH)₂, the peaks at around 532.62, 531.79 and 530.85 eV were corresponded to Zr—O—C, Zr—OH and O—Ca, respectively (Fig. 3(VIII)). The peaks at around 284.21, 286.07 and 287.82 eV were resembled to C—O, Zr—O—C and C—OH/C=O, respectively (Fig. 3(IX)). Among them, Zr—O—C, C—OH/O—H and C—O are the characteristic alps of MOFs-NPs, SA, and GA which represented the manifestation of hydroxyl and carboxyl groups in the MCs. Noticeably, the characteristics peak of Zr—O—C in the high resolution XPS spectra of O 1s and C 1s hinted the successful interaction of MOFs-NPs with the hydrophilic functional groups of SA and GA in/on the MCs [58,59]. In addition, the Zr—OH bond peak in the high resolution XPS spectra of O 1s clearly hinted that MOFs-NPs contained more uncoordinated Zr—OH bonds and can provide stronger Lewis acid-base interaction for the adsorption of metal ions [47]. The characteristic peak of O—Ca confirmed the formation of ionic bonding between Ca²⁺ and carboxyl/-COOH groups of SA. Besides, the peaks at around 184.6/184.43 and 182.2/182.02 eV were assigned to Zr 3d_{3/2} and Zr 3d_{5/2} of Zr element, respectively, which can be corresponded to Zr—O bonds of UiO-66-OH/(OH)₂, respectively, supporting the presence of Zr⁴⁺ for zirconium-oxo cluster [46,60–62] (Fig. S2(V-VI)). Overall, the presence of Zr peak hinted the successful assimilation of MOF-NPs

in/on the 3-D SGMMCs-OH/(OH)₂. The findings demonstrated that the relative atomic fractions (as attained by the XPS quantification for 3-D SGMMCs-OH) were O (53.48 %), C (30.77 %), Ca (10.06 %), Zr (3.51 %) and Na (0.02). Similarly, the relative atomic percentages (as acquired by the XPS quantification for 3-D SGMMCs-(OH)₂) were O (39.94 %), C (55.98 %), Ca (3.31 %), Zr (0.79 %) and Na (0.01) (Table SIII). The presence of Na 1s peak indicated that some of the —COONa radicals (of SA) might not participate in the crosslinking reactions. Therefore, the as-prepared 3-D SGMMCs-OH/(OH)₂ with IPNs configuration acquired not only a suitable chemical stability, but also abundant “vacant/active sites” (-COOH and -OH) for the eradication of hazardous environmental pollutants.

3.1.3. Morphological analysis of the 3-D SGMMCs-OH/(OH)₂

SEM analysis was performed to comprehend the morphology of the as-synthesized 3-D SGMMCs-OH/(OH)₂, and to confirm the manifestation of incorporated MOF-NPs. At first, the morphology of UiO-66-OH and UiO-66-(OH)₂-MOF-NPs were explored by SEM investigations, and it revealed aggregates of polygonal-shaped particles with a size range of about 50–60 nm and 150–300 nm, respectively, as previously recognized by dynamic light scattering (DLS) technique (Fig. 4I&II(a)) (Fig. S2(II-III)). The freeze-dried 3-D SGMMCs-OH/(OH)₂ had noticeable 3-D honeycomb porous configuration (Fig. 4I&II(b)). The as-synthesized capsules occupied top dense, porous screen mesh, undulated and rough channel like architecture (Fig. 4I&II(A-B)). Some snaps or ruptures were also observed on the surface of the capsules, along-with the manifestation of diverse series of apertures diameter from the upper layer to inner crux that elucidates the high permeability and porosity of the capsules (Fig. 4I&II(B)). In fact, the pore sizes depleted from small to large, which steadily matured inward and depicted a hierarchical structure, which indicated the uneven cross-linking reaction ratio between the surface and inner of the liquor globule during the fabrication process. Overall, the as-prepared 3-D SGMMCs-OH/(OH)₂ depicted a micro-porous capsule ‘shell’ to macro-porous core configuration (Figs. 4I&II(A-B)). The presence of pores in the kernel revealed the manifestation of high-water content, resulting comparatively higher surface area and spongy pattern of SA-GA-UiO-66-OH/(OH)₂ (Fig. 4D). Noticeably, the UiO-66-OH and UiO-66-(OH)₂ MOF crystals were spotted from outer surface to inner core of the capsule, which clearly demonstrated the homogenous distribution of MOF-NPs in the as-synthesized capsules (Fig. 4I&II(A-B)). The morphology of 3-D SMCs was also compared with the loaded capsules and the findings clearly illustrated that the MOF-NPs were successfully attached in the as-developed capsules (Fig. 4I&II(c&B)).

This morphology can be elucidated in this way that a porous solid phase style shell-nuclei was developed as a spherical liquid droplet (of SA-UiO-66-OH/(OH)₂ MOF matrix) swiftly infused into initial cross-linking agent solution (CaCl₂). In the beginning, a dense, re-entrant, compact, and microporous screen mesh type structure was formed because of the utilization of -COOH and -OH functional groups by the interface of SA with Ca²⁺ and UiO-66-OH/(OH)₂ MOF-NPs. As the upper layer developed, a tumble was established between leading crosslinking agent and SA-UiO-66-OH/(OH)₂ MOF matrix to create inner core. However, the nano-holes/pores and interspaces were noticed in the core/kernel of the 3-D SGMMCs-OH/(OH)₂, which indicated unequal polymerization rate between SA-UiO-66-OH/(OH)₂ MOF matrix and primary crosslinking agent due to the leakage of solution or lack of penetration of primary crosslinking agent into the core because of capsule ‘shell’, that directed to the enhancement of the pore size. Moreover, the attachment/coating of UiO-66-OH/(OH)₂ MOF-NPs with the interspaces and channel surfaces was also noticed, which clearly suggested the crosslinking of UiO-66-OH/(OH)₂ MOF-NPs with the SA via hydrogen bonding (Fig. 5). In addition, secondary crosslinking agent (GA) performed an imperative job in refashioning the capsules morphology by developing a slacker and macroporous configuration in the kernel, which additionally improved the compactness of apertures

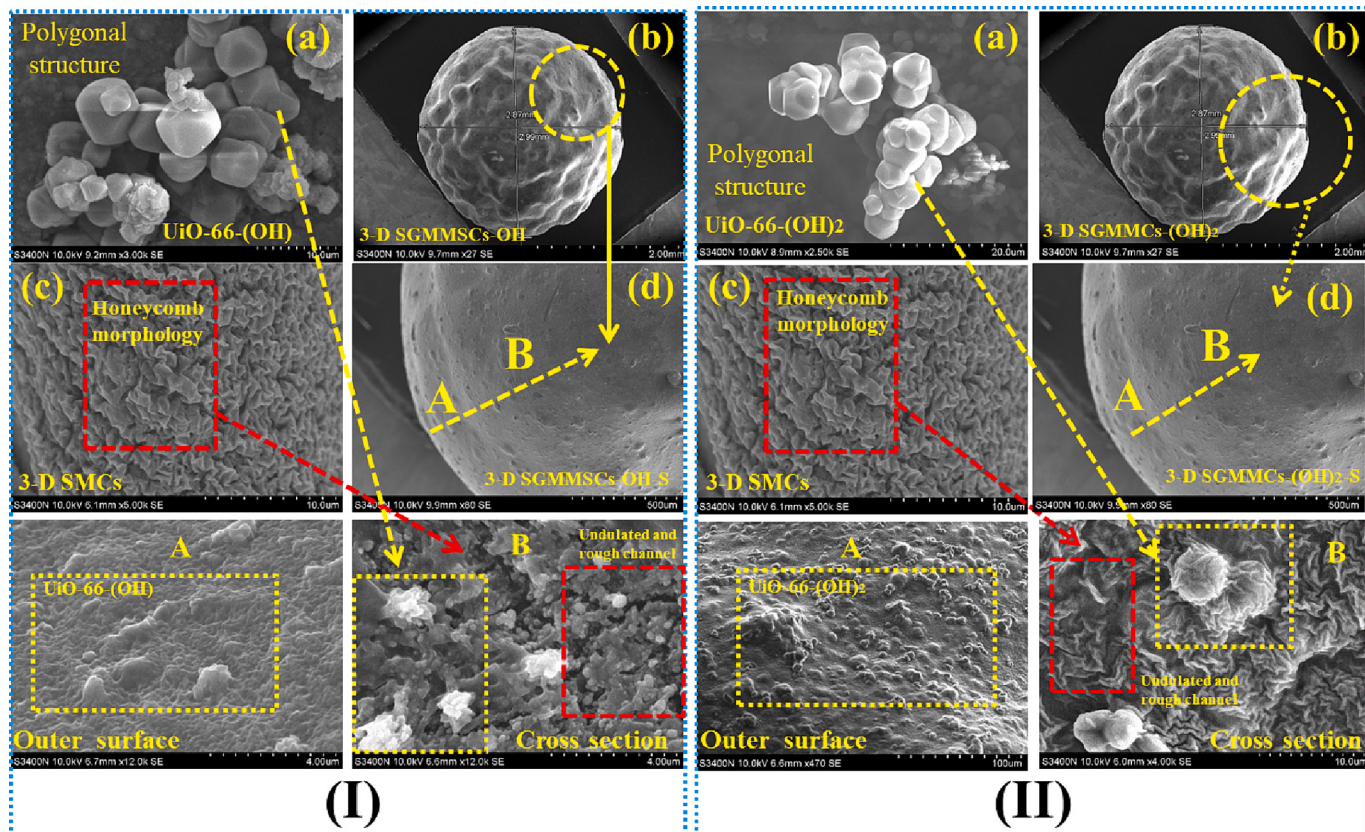


Fig. 4. (I) SEM micrographs of (a) UiO-66-OH, (b) 3-D SGMMCs-OH, (c) 3-D SMCs, (d) 3-D SGMMCs-OH-S, (A) outer surface of the 3-D SGMMCs-OH, and (B) cross section of the 3-D SGMMCs-OH; and (II) SEM images of (a) UiO-66-(OH)₂, (b) 3-D SGMMCs-(OH)₂, (c) 3-D SMCs, (d) 3-D SGMMCs-(OH)₂-S, (A) outer surface of the 3-D SGMMCs-(OH)₂, and (B) cross section of the 3-D SGMMCs-(OH)₂.

and mechanical properties. Notably, the spongy macroporous to microporous 3-D structure would enhance the trapping and twinkling of pollutants within kernel linkage by developing pore's channel, which will eventually improve the sorptive capability of the sorbent by creating additional active or vacant sites for the sorption of pollutants. The conceptual possible crosslinking networks of SA-CaCl₂, SA-GA-MOF-NPs and SA-GA are elucidated in Fig. 5.

3.2. Optimization of stability and applicability of 3-D SGMMCs-OH/(OH)₂ for the eradication of PTMs

3.2.1. Stability of 3-D SGMMCs-OH/(OH)₂

The pH_{PZC} values of the UiO-66-OH-MOF-NPs, UiO-66-(OH)₂-MOF-NPs, 3-D SMCs, 3-D SGMMCs-OH and 3-D SGMMCs-(OH)₂ were 4.75, 4.10, 3.06, 3.95 and 4.89, respectively (Fig. S4(I)), as estimated by pH drift method (Text SI). The swelling ratio (SR) of 3-D SGMMCs-OH/(OH)₂ significantly improved with the increase of solution pH from 1 to 10, and then it was slightly dropped when the pH was further increased from 10 to 14 (Fig. 6(I)). On the other hand, the color of solution was varied from colorless to light yellowish with the increase of solution pH from 1 to 14 (Fig. S1), indicating the leaching of loaded MOF at pH > 10 due to the destabilization of the crosslinking interaction between MOF-NPs SA-GA matrix because the swelling behavior enhanced the overall micro-porosity of the capsule, which facilitated in the easy release of MOFs-NPs from capsule via weakening the subsisted H bonding at higher pH. Thus, the loading of MOF-NPs was stable up-to pH 10 due to the formation of crosslinking interactions between MOF-NPs and SA-GA matrix via hydrogen bonding, as previously ensured by FTIR and XPS analyses. In addition, the loading of MOFs-NPs significantly increased SR (33.18 & 50.10 %) of 3-D SGMMCs-OH and 3-D SGMMCs-(OH)₂, respectively, compared to un-loaded capsules 3-D SMCs (Fig. S4(II)).

3.2.2. Effect of MOFs NPs content

Fig. 6 (II) depicts the influence of MOF-NPs content on the elimination of PTMs by 3-D SGMMCs-OH/(OH)₂. The removal of PTMs was initially improved by the increasing MOF content up to 70 & 60 wt% in the 3-D SGMMCs-OH and 3-D SGMMCs-(OH)₂, respectively. This upsurge in ejection efficacy might be owing to the convenience of superior vacant sites, (-COOH and -OH functional groups) in the 3-D SGMMCs-OH/(OH)₂ or the manifestation of superior surface area for the sorption of PTMs. On average, 96 and 97 % of removal was observed for Cd²⁺ and Cu²⁺, respectively, at 70 wt% MOF loading into 3-D SGMMCs-OH. Likewise, on average, 97 and 99 % of removal was observed for Cd²⁺ and Cu²⁺, respectively, at 60 wt% MOF loading into 3-D SGMMCs-(OH)₂. While, when the content of MOF was >70 & 60 wt%, the eradication of PTMs was significantly dropped. This can be explained in this way that the equilibrium point was accomplished between MOF-NPs and SA-GA matrix at 70 & 60 wt% MOF loading, and all the SA-GA vacant sites crosslinked with MOF-NPs during fabrication. While, by further increase in the MOF content (>70 & 60 wt%), the un-crosslinked MOF-NPs were percolated from the capsules and altered the color of solution from colorless to light yellowish (Fig. S1). Similarly, during the sorption of PTMs, the sorption performance was initially improved because of the deprotonation of -OH and -COOH groups; however, later, the leaching of MOF-NPs declined the convenience of surplus unoccupied/active sites on/in the capsules, which eventually inhibited the removal performance. Likewise, the higher MOF contents did enhance aggregation in the SA-GA matrix which resulted in reducing the surface area, reduction in the diffusion of PTMs into the inner pores of the capsules followed by lessening the accessible vacant sites for metal cations sorption. Therefore, 70 & 60 wt% MOF contents were an optimum loading rate into 3-D SGMMCs-OH and 3-D SGMMCs-(OH)₂ to keep cost effective synthesis protocol as well as to get highest removal of

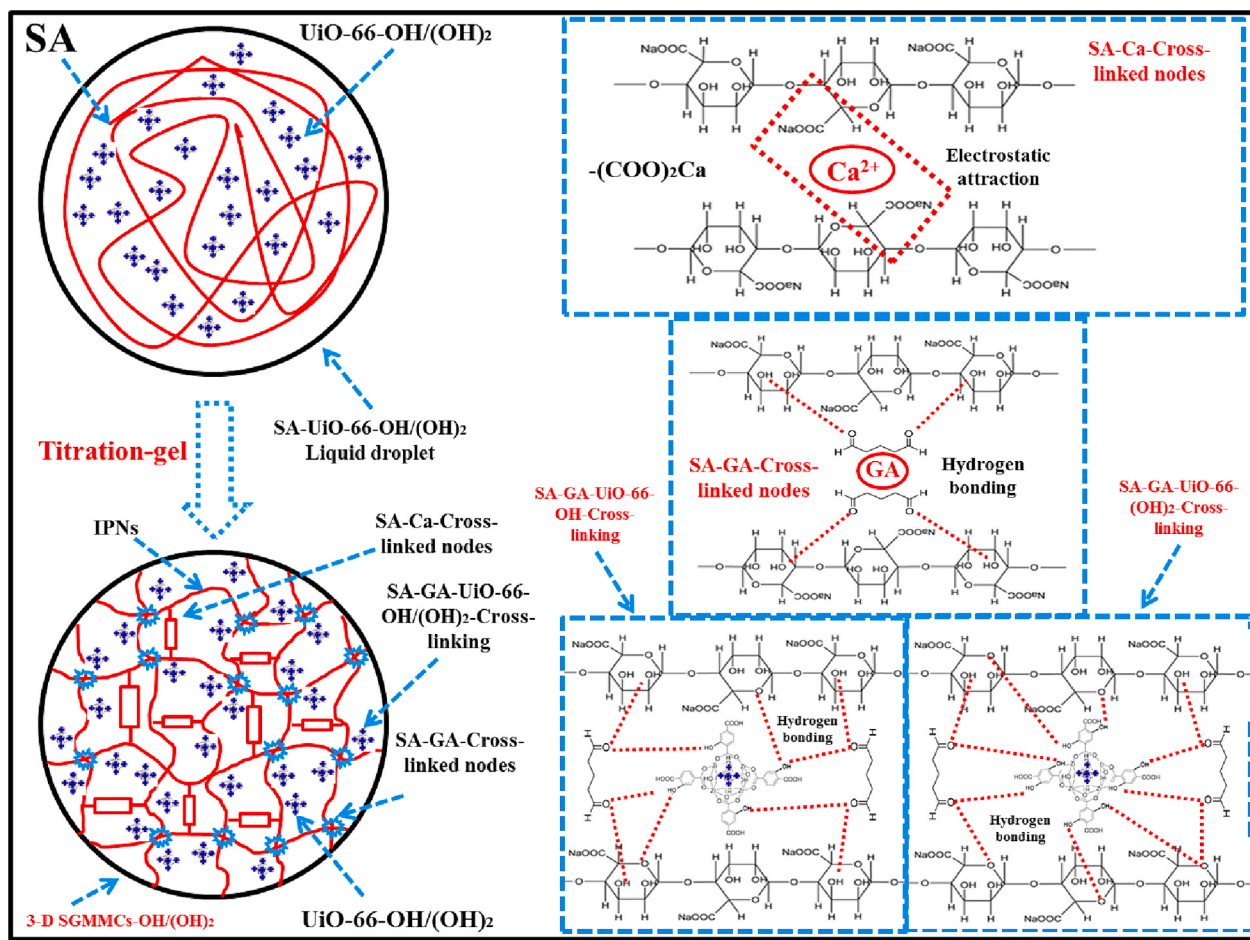


Fig. 5. Conceptual possible crosslinking networks of sodium alginate and MOF nanoparticles during fabrication of 3-D SGMMCs-OH/(OH)₂ such as SA-CaCl₂; SA-GA-UiO-66-OH; SA-GA-UiO-66-(OH)₂; and SA-GA.

PTMs. In addition, the pH of the solution was slightly declined by increasing MOF contents (from 1 to 100 wt%), which also disclosed the leaching of MOF particles from capsules (Fig. S4(III)).

3.3. Optimization of pertinent operating parameters on the eradication of PTMs by 3-D SGMMCs-OH/(OH)₂

3.3.1. Effect of adsorbent dosage

The eradication competences of all the examined metal ions were boosted from 10 to >90 % by the increased capsules dosage from 0.001 to 0.01 g/L, and then it was steady by extra boosting the 3-D SGMMCs-OH/(OH)₂ dose from 0.01 to 0.05 g/L (Fig. 6(III)). This surge in eradication might be owing to the availability of greater unoccupied sites on/in the 3-D SGMMCs-OH/(OH)₂ or manifestation of higher surface area [63]. On average, 95/(97) and 97/(98) % of eradication was observed for Cd²⁺ and Cu²⁺, respectively, by employing 3-D SGMMCs-OH/(OH)₂ dose of 0.01 g/L. Hence, 0.01 g/L dose of capsules was chosen as an optimal amount for further trials.

3.3.2. Effect of solution pH

The stimulus of pH on the performance of 3-D SGMMCs-OH/(OH)₂ was examined in the range of pH 1–8 because the solution pH can alter the surface charges, chemical interaction, cross-effects on metal speciation and protonation/deprotonation of hydrophilic functional groups (-COOH and -OH). The removal efficiencies of Cu²⁺ and Cd²⁺ were maximum at pH 6 (Figs. 6(IV) & S4(IV)). Initially, the ejection of both Cd²⁺ and Cu²⁺ were boosted by increasing pH from 1 to 6, and later it was feebly declined after pH increase from 7 to 8. It is well-recognized

that at various pH values, both Cd²⁺ and Cu²⁺ exists in diverse fragments, i.e., Cd²⁺/Cu²⁺, Cd(OH)⁺/Cu(OH)⁺ and Cd(OH)₂/Cu(OH)₂ which could influence on the ejection efficiency [64,65]. In the present study, first at lower pH (1–4), the protonation functional groups (-OH and -COOH) established Coulombic repulsion between Cd²⁺/Cu²⁺ or Cd(OH)⁺/Cu(OH)⁺ and positively charged 3-D SGMMCs-OH/(OH)₂ because of higher number of protons (H⁺) potency, leading to the inhibited ejection proficiency of cationic metals. While, at higher pH (4–8), the quantity of (H⁺) was less, which reduced the revolting interactions, and meanwhile enhanced the attractions between adsorbent and adsorbate by the hydrogen bonding along-with ion-exchange mechanism, because Cd²⁺ and Cu²⁺ subsisted in Cd²⁺/Cu²⁺, Cd(OH)⁺/Cu(OH)⁺ and Cd(OH)₂/Cu(OH)₂ forms in the solution, and consequently, a higher eradication of metals cations was perceived. On the other hand, the pH_{PZC} of the 3-D SGMMCs-OH and 3-D SGMMCs-(OH)₂ was 3.95 & 3.89, respectively, and hence at pH < pH_{PZC}, the surface of the 3-D SGMMCs-OH/(OH)₂ was positively charged thus enhancing the electrostatic repulsion and in the meantime, the manifestation of greater quantity of H⁺ potency in the emulsion competed the metals cations for active sites, which ultimately inhibited the sorption of metals cations by 3-D SGMMCs-OH/(OH)₂. Moreover, at pH > pH_{PZC}, the surface of the 3-D SGMMCs-OH/(OH)₂ was negatively charged, so encouraging electrostatic interaction with metal cations and sorbent, which ultimately enhanced the eradication of metal cations by 3-D SGMMCs-OH/(OH)₂. But, the elimination of metal cations declined again after pH 6 because of the probable precipitation of metals cations or constellation influence between metals cations and OH⁻, as previously narrated [34,66–68]. Therefore, the pH 6 was kept as an optimal for Cu²⁺ and Cd²⁺.

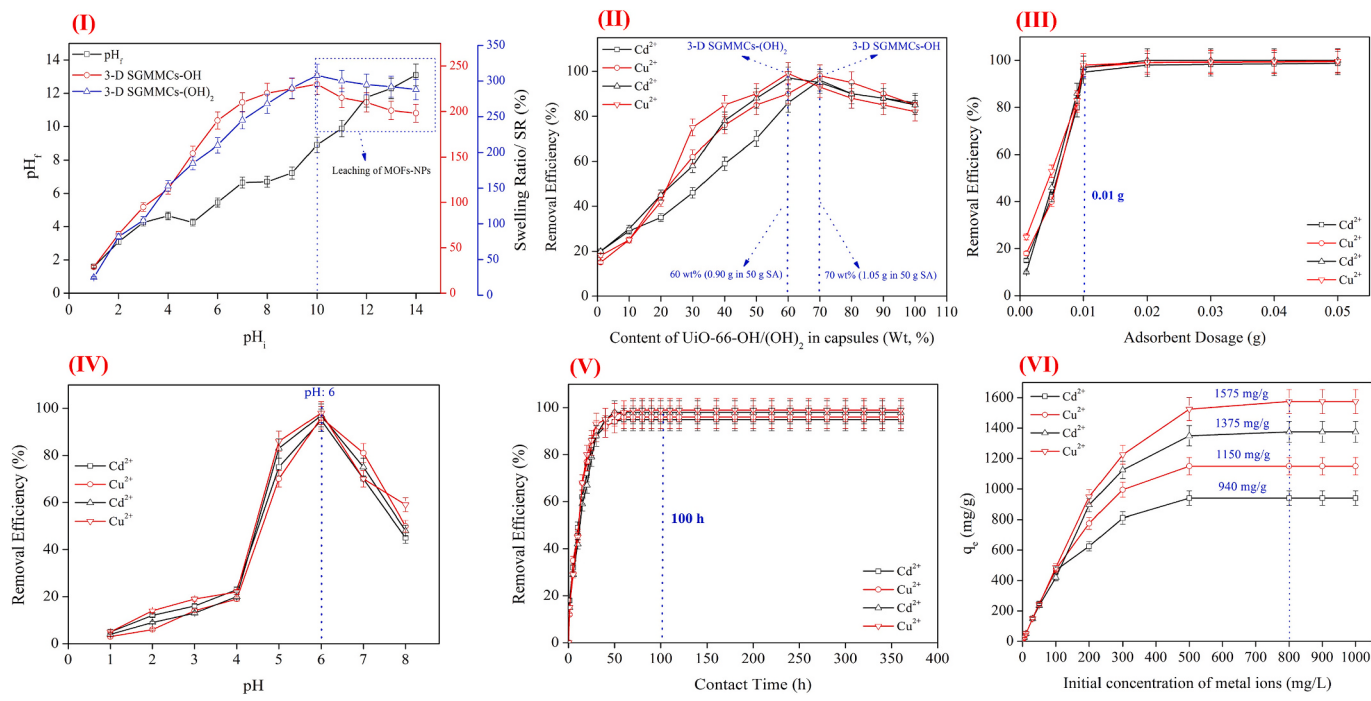


Fig. 6. (I) stability and swelling ratio of 3 D SGMMCs-OH/(OH)₂ in the pH range of 1–14 [Dosage = 0.01 g; Co = 20 mg/L (0.1 M NaCl); pH = 1–14, temperature = 298.15 K; contact time = 0–48 h; agitation = 130 rpm]; (II) optimization of content of loaded MOF-NPs in term of PTMs removal; influence of various operating parameter on the adsorptive performance of 3 D SGMMCs-OH/(OH)₂ in the removal of PTMs in single system (III) doses of capsules [dosage = 0.001–0.05 g; C₀ = 100 mg/L (TPMs); pH = 6, temperature = 298.15 K; contact time = 48 h; agitation = 130 rpm]; (IV) solution pH [Dosage = 0.01 g; Co = 50 mg/L (PTMs); pH = 1–14, temperature = 298.15 K; contact time = 0–48 h; agitation = 130 rpm]; (V) contact time [Dosage = 0.01 g; Co = 50 mg/L (PTMs); pH = 6, temperature = 298.15 K; contact time = 0–360 h; agitation = 130 rpm]; and (VI) initial metal cations concentration (mg/L) [Dosage = 0.01 g; Co = 0–1000 mg/L (PTMs); pH = 6, temperature = 298.15 K; contact time = 0–120 h; agitation = 130 rpm].

subsequent experiments.

3.3.3. Effect of contact time, initial pollutants concentration and temperature

As depicted in Fig. 6(V), the eradication of metals ions appeared in two phases in the time range of 0–360 h. The first phase was quick and > 80 % of the metal ions eliminated within the first 40 h. The second phase was moderate and reached to steadiness until utmost eradication was achieved. This logic is understandable, as numerous researchers narrated same phenomenon [5,19]. Thus, the optimal equilibrium time was 100 h. In addition, the equilibrium time of 3-D SMCs was also investigated by keeping similar experimental conditions, and it was found to be 80 h (Fig. S4(V)). Overall, the removal efficiencies were followed the order as: 3-D SGMMCs-(OH)₂ > 3-D SGMMCs-OH > 3-D SMCs, at equilibrium time, which clearly implied that the loaded of MOF particles significantly increased the hydrophilic functional groups on/in the capsules. Further, the sorption capacities/performance of metal ions was at first rapidly increased with the rise of metals ions from 5 to 300 mg/L, and then approached equilibrium/saturation. On average, the estimated sorption capacities of Cd²⁺ and Cu²⁺ by 3-D SGMMCs-OH were 940 and 1150 mg/g, respectively (Fig. 6(VI)). Moreover, the eradication efficiency of both metal ions was improved with the rise of reaction temperature from 298.15 to 333.15 K (Fig. S4(VI)), which recommended that the elimination was spontaneous and exothermic in nature [69].

3.4. Adsorption kinetics

Sorption kinetics permits fixing the equilibrium time but also assess the steps that are governing the passage of the solute form the suspension to the adsorbent surface. The experimental kinetic data were depicted by Pseudo-first order, Pseudo-second order, Intraparticle

diffusion, Liquid film diffusion and Elovich dummies to acquire the kinetic and removal process of PTMs by 3-D SGMMCs-OH/(OH)₂. As shown in the Table SIV-V, the assessments of regression coefficient ($R^2 > 0.99$) revealed that the sorption date of PTMs in the 3-D SGMMCs-OH/(OH)₂ were well matched with pseudo-second-order kinetics model and thus indicating the presence of chemisorption and/or ion-exchange mechanism (Fig. 7(I-II)). In addition, the estimated quantities of q_e did not diverge much from the experimental assessments. In contrast, the assessments of k_2 were slighter than as associated to h , which suggested that at first there is a quick sorption of PTMs and subsequently later comprehended by gentle sorption [70]. The findings of other models have been documented in the supplementary information (Text-SV).

3.5. Adsorption isotherm

Four isotherm models including Langmuir, Freundlich, Temkin and Dubinin-Radushkevich isotherms were considered to elucidate the metal ions interface by 3-D SGMMCs-OH/(OH)₂ (Table VI). The findings depicted that the adsorptive capacity boosted with the rise of initial concentration of PTMs and then reached to equilibrium. It can be noticed in Fig. 7(V), the Langmuir model represented the best corresponded to the experimental statistics of metal ions sorption in the 3-D SGMMCs-OH/(OH)₂ with a higher regression coefficient ($R^2 > 0.97$), indicating the monolayer sorption of PTMs in the 3-D SGMMCs-OH/(OH)₂. Besides, the values of K_L indicated that adsorption was favorable and promising [71]. The maximum monolayer adsorption capacities of Cd²⁺ and Cu²⁺ (by 3-D SGMMCs-OH) were 940 and 1150 mg/g, respectively. While, the estimated sorption capacities of Cd²⁺ and Cu²⁺ (by 3-D SGMMCs-(OH)₂) were 1375 and 1575 mg/g, respectively (Table VI). Generally, the evidence acquired from the isotherm and kinetic assessments along-with the reality that PTMs and reactive

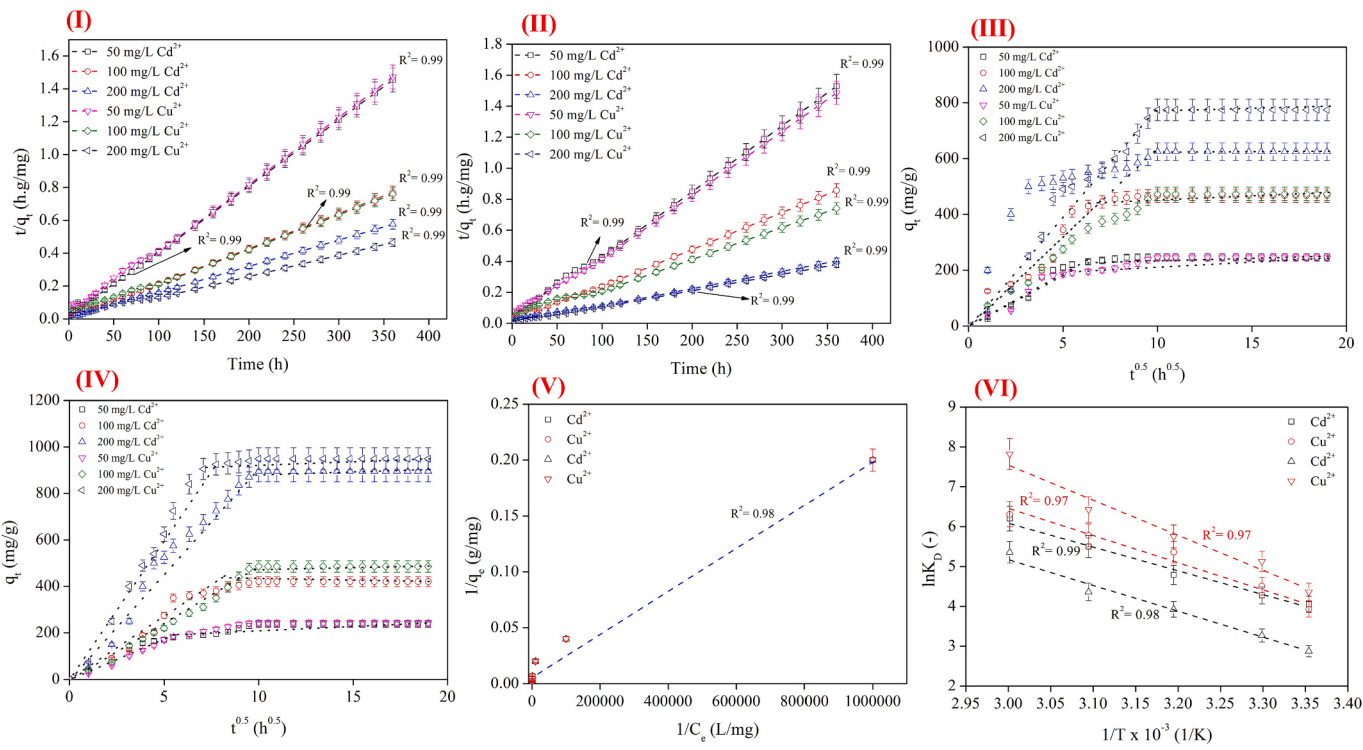


Fig. 7. The linear plot of pseudo-second-order model of the targeted PTMs by (I) 3-D SGMMCs-OH and (II) 3-D SGMMCs-(OH)₂; the liner plot of Intraparticle diffusion model of the targeted PTMs by (III) 3-D SGMMCs-OH and (IV) 3-D SGMMCs-(OH)₂; [dosage = 0.01 g; Co = 50–200 mg/L (PTMs); pH = 3, 5 & 6, temperature = 298.15 K; contact time = 0–120 h; agitation = 130 rpm]; (V) the linear plot of Langmuir isotherm model for Cd²⁺ and Cu²⁺sorption on/in the 3-D SGMMCs-OH and 3-D SGMMCs-(OH)₂ [Dosage = 0.01 mg; Co = 0–1000 mg/L (PTMs); pH = 3, 5 & 6, temperature = 298.15 K; contact time = 0–120 h; agitation = 130 rpm]; and (VI) thermodynamic plots for the sorption of PTMs by 3-D SGMMCs-OH and 3-D SGMMCs-(OH)₂ in the range of temperature from 298.15 to 333.15 K.

functional groups devoted in the 3-D SGMMCs are oppositely charged, recommending the ion-exchange might governing sorptive mechanisms of PTMs by 3-D SGMMCs-OH/(OH)₂.

3.6. Thermodynamic studies

The thermodynamic results are displayed in Table SVII and Fig. 7 (IV). The negative values of Gibbs free energy (ΔG°), enthalpy (ΔH°), and standard entropy (ΔS°) hinted the thermodynamically feasible spontaneous and exothermic nature of PTMs sorption in the 3-D SGMMCs-OH/(OH)₂ temperature range of 298.15–333.15 K. In addition, the assessments of ΔG° were improved as the temperature enhanced, which suggested a superior probability of sorption at the elevated temperature [64]. Notably, the values of ΔH° were higher than 20.9 KJ/mol, which hinted that the PTMs attached on/in the 3-D SGMMCs-OH/(OH)₂ via ion-exchange/chemisorption mechanism, as earlier confirmed by isotherm and kinetics surveys. In contrast, the negative assessments of ΔS° evoked a reduction in adsorbed species level of liberty at the solid-solution boundary throughout the complete sorption activity [63,72].

3.7. Selectivity performance

The sorbents had a great selectivity to eradicate cationic metals ions (Fig. 8(I)). At pH 6, the sorbents had a good selectivity against Cu²⁺ in the presence of other metals ions such as Cr(VI), Cr³⁺, Cd²⁺, Zn²⁺, Mg²⁺ and Na⁺. This was owing to the demonstration of deprotonated reactive functional groups such as -OH and -COOH in the 3-D SGMMCs-OH/(OH)₂ at pH 6, which were favorable to interact with the cationic metals ions than anionic Cr species via electrostatic interactions and ion-exchange mechanism. Overall, the selectivity sequence followed as: Cu²⁺ > Zn²⁺ > Cd²⁺ > Mg²⁺ > Cr³⁺ > Na⁺ > Cr(VI). The low

eradication efficiency of Cu²⁺ and Cd²⁺ (compared to single-metal solutions) might be owing to the interference by the metals with low empathy to reactive functional group/(-COOH of alginate), which inhibited the crosslinking process of targeted metals with the active sites of the sorbent, as similar findings were reported previously [71,73–75].

3.8. Reusability of 3-D SGMMCs-OH/(OH)₂

The discussions about reusability of 3-D SGMMCs are demonstrated in supplementary information (Text SIV). As presented in Fig. S5, the 3-D SGMMCs-OH/(OH)₂ maintained its effectiveness up-to six (06) successive treatment rotations. Notably, it was observed that only 5–8 % reduction in eradication efficiency was observed up-to six (06) consecutive treatment cycles.

3.9. Proposed removal mechanism

The FTIR, EDX/S and XPS analyses were employed to investigate the sorption mechanism of PTMs by 3-D SGMMCs-OH/(OH)₂. First, the FTIR spectrum was acquired after the sorption of PTMs by 3-D SGMMCs-OH/(OH)₂ (Fig. 8(II-III)). The findings indicated four main variations at around 3600–3200 cm⁻¹ and 1700–1300 cm⁻¹, 1201–1234 cm⁻¹, and 600–800 cm⁻¹, which can be allocated to the alterations of reactive functional groups (-COOH and -OH). The single prominent peak at 3485 cm⁻¹ of -O⁻ stretching shifted to a lower wavenumber of 3475 and 3473 cm⁻¹ after the sorption of Cd²⁺ and Cu²⁺, respectively, which illustrated that -O⁻ groups worked as binding sites for PTMs, as also stated in previously published reports [76,77]. Likewise, the peaks at 1611 cm⁻¹ and 1413 cm⁻¹ of -COO⁻ group shifted to a lower wavenumber of 1599 cm⁻¹ and 1406 cm⁻¹ after the sorption of Cd²⁺ and Cu²⁺, respectively, which illustrated that -COO⁻ groups worked as binding sites for PTMs, as also reported in previously published reports

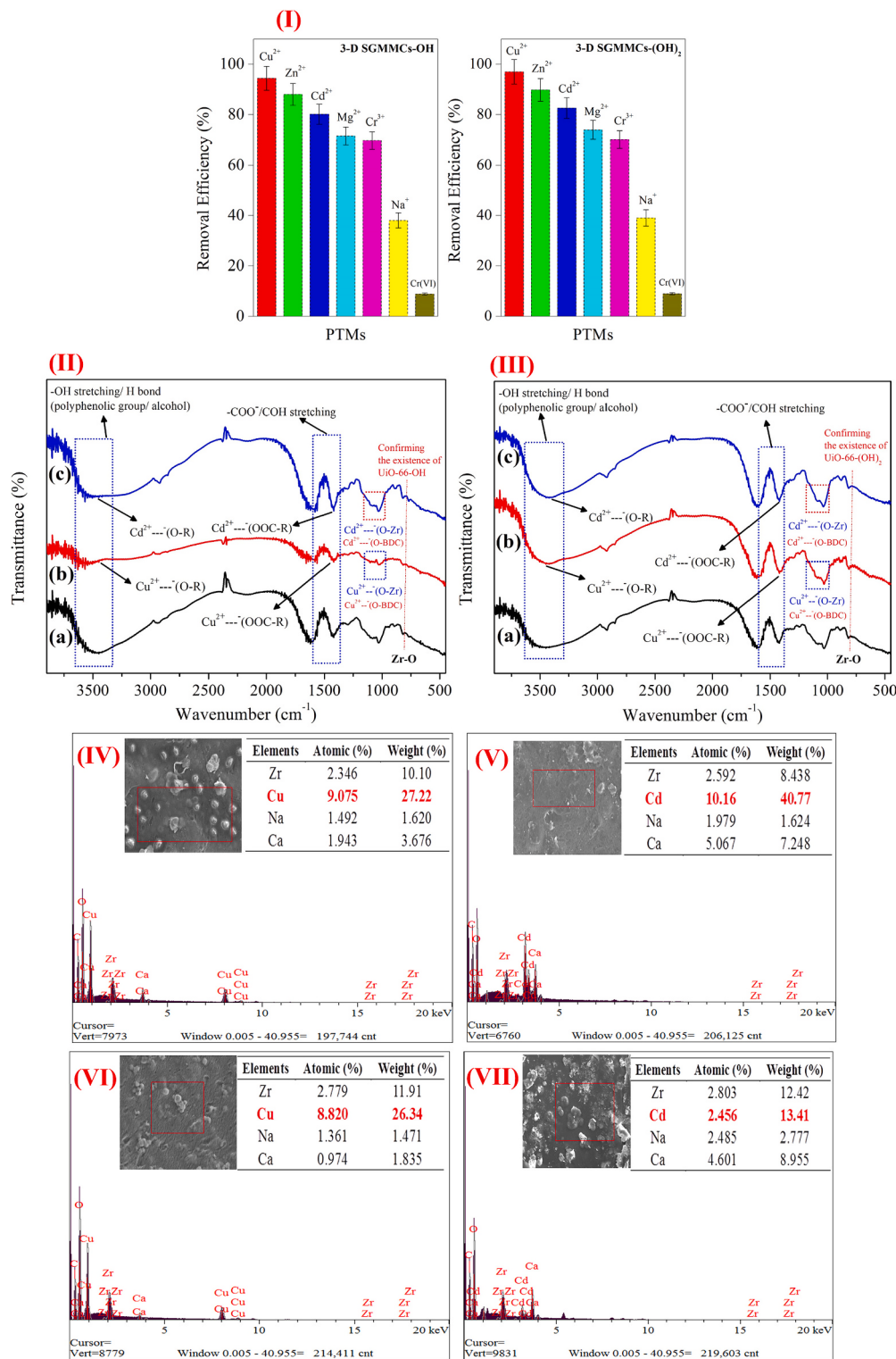


Fig. 8. (I) Selectivity performance of 3-D SGMMCs-OH and 3-D SGMMCs-(OH)₂ [dosage = 0.01 g; Co = 10 mg/L (PTMs); pH = 6, temperature = 298.15 K; contact time = 0–120 h; agitation = 130 rpm], (II) the FTIR spectra of (a) 3-D SGMMCs-OH before and after the adsorption of (b) Cu²⁺, (c) Cd²⁺; (III) the FTIR spectra of (a) 3-D SGMMCs-(OH)₂ before and after the adsorption of (b) Cu²⁺, (c) Cd²⁺, the EDX/S spectra of 3-D SGMMCs-OH after the adsorption of (IV) Cu²⁺, (V) Cd²⁺; the EDX/S spectra of 3-D SGMMCs-(OH)₂ after the adsorption of (VI) Cu²⁺, (VII) Cd²⁺.

[78–80]. Notably, it can be noticed that the peaks at around 1055–1150 cm⁻¹ related to the bending vibrations of hydroxyl groups on metal oxide clusters (Zr-OH) became much less obvious after adsorption of Cd²⁺ and Cu²⁺, respectively, which hinted the attachment of metal ions with the hydroxyl group of Zr-O-H bond to develop a Zr-O-Cd²⁺/Cu²⁺

coordination bond, releasing H⁺ and hydroxyl groups to form water to maintain charge balance in the solution [22,60]. Similarly, the Zr-O-C connection between Zr and BDC-OH/(OH)₂ aromatic ligands/linkers could help in the adsorption process by exchanging some BDC ligands with metal ions because the hydroxyl groups on membrane capsules are

considered the primarily responsible for the adsorption of metal ions [44,81]. In addition, the peaks at 805 cm^{-1} and 680 cm^{-1} (of Zr-O) were slightly skewed, which clearly suggested that the loaded MOF-NPs participated in the adsorption of Cd^{2+} and Cu^{2+} by membrane capsules [47,82]. Overall, these changes indicated the sorption of PTMs on/in the 3-D SGMMCs-OH/(OH)₂ via electrostatic interaction, ion-exchange, inner-sphere coordination bonds/interactions, and aromatic ligands exchange mechanism, e.g., (R-O)⁻... Cu^{2+} , (R-COO)⁻... Cu^{2+} , (R-O)⁻... Cd^{2+} , (R-COO)⁻... Cd^{2+} , (Zr-O)⁻... Cu^{2+} , (Zr-O)⁻... Cd^{2+} , (BDC-O)⁻... Cu^{2+} , and (BDC-O)⁻... Cd^{2+} [72]. Secondly, the EDX/S spectrums were also acquired, and the findings indicated the existence of Cu^{2+} and Cd^{2+} , which ensured the sorption of PTMs in the as-developed capsules. Furthermore, a decline in the atomic percentages of C and O elements was observed after the sorption of PTMs, which hinted the consumption of -COOH and -OH functional groups during sorption process (Figs. 8 (IV-VII) & S6(I-IV)).

Moreover, the XPS results showed that after the sorption of PTMs, two new peaks of Cu 2p and Cd 3d emerged at 931.33/932.96 and 404.97/405.74 eV, respectively, indicating that Cu^{2+} and Cd^{2+} were

adsorbed on/in the 3-D SGMMCs-OH/(OH)₂ (Fig. 9(I-II)). Further, the high-resolution spectra of PTMs were also explored to fully understand the adsorptive mechanism (Fig. 9(III-IX)). In case of 3-D SGMMCs-OH, two main peaks at around 404.97 and 411.63 eV emerged in the XPS contour of Cd 3d, which can be allocated to the Cd^{2+} binding energy of $3\text{d}_{5/2}$ and $3\text{d}_{3/2}$ deviations, respectively [83-85]. The energy difference was 6.66 eV [86]. The Cd $3\text{d}_{5/2}$ and Cd $3\text{d}_{3/2}$ characteristic peaks appeared at 406.03 and 412.09 eV, respectively and these peaks can be associated to Cd^{2+} -X or $\text{Cd}-\pi$ bonding supported by C=C [87-89], while the other peaks at 404.97 and 411.63 eV reflected the coordination interaction of Cd^{2+} with the oxygen containing functional groups (-OH, -COOH) of the membrane capsules to form Cd—O bonding [90-92]. The manifestation of these peaks in XPS spectra ensured that Cd^{2+} particles were effectively adsorbed onto/in the membrane capsules (Fig. 9(III)). Furthermore, the high-resolution spectra of O 1s depicted that the binding energy of oxygen-containing groups changed from 532.52 to 530.49 eV, which ensured the contribution of hydrophilic groups (C=O, —OH and C—O) in the sorption of Cd^{2+} on/in the sorbent via electrostatic attraction and/or ion-exchange mechanism. Noticeably, the

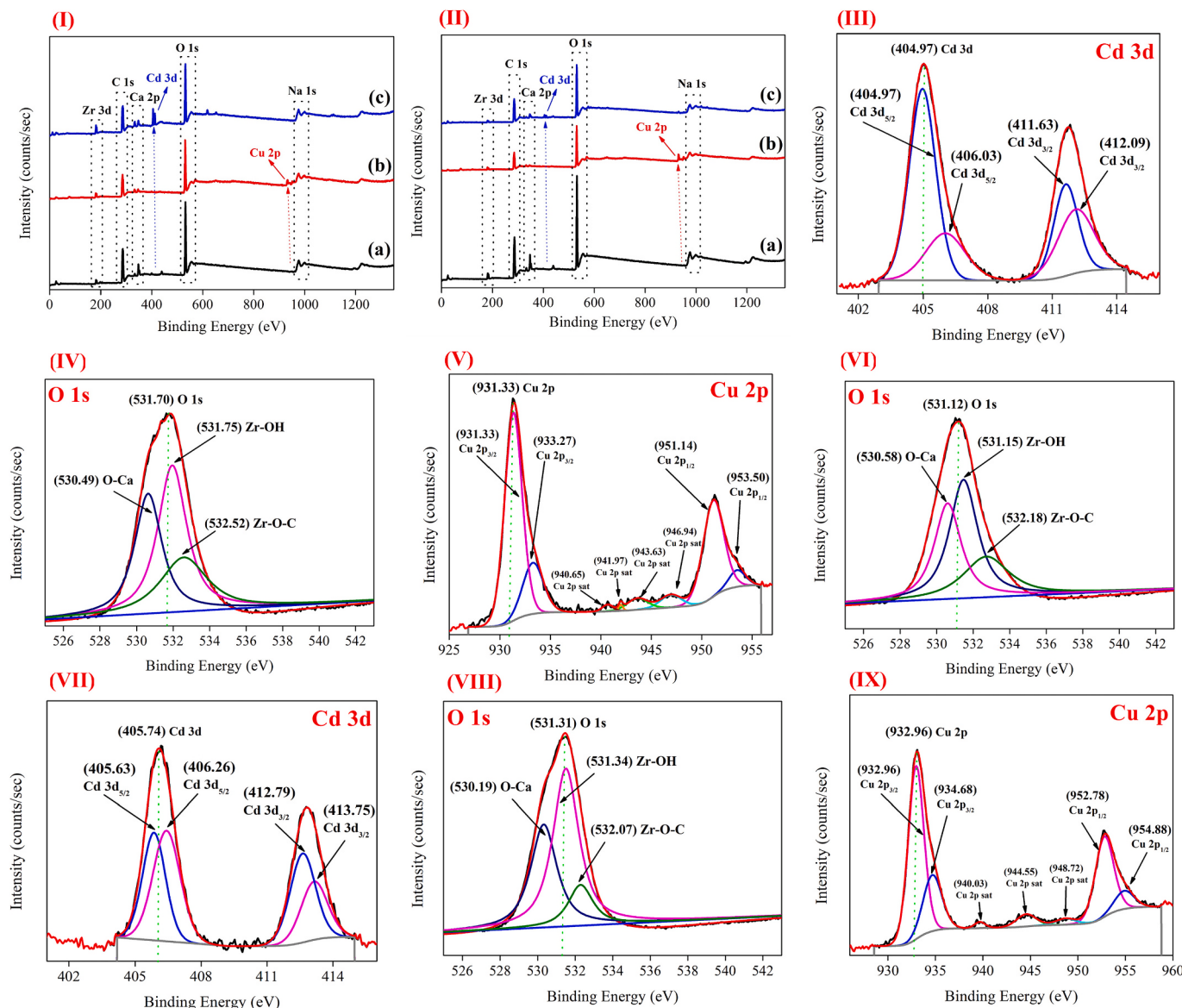


Fig. 9. (I) XPS spectra of (a) 3-D SGMMCs-OH before, and after the adsorption of (b) Cu^{2+} , and (c) Cd^{2+} ; (II) XPS spectra of (a) 3-D SGMMCs-(OH)₂ before, and after the adsorption of (b) Cu^{2+} , and (c) Cd^{2+} ; High resolution XPS spectra of (III) Cd 3d, (IV) O 1s, after the sorption of Cd^{2+} , (V) Cu 2p, and (VI) O 1s after the sorption of Cu^{2+} by 3-D SGMMCs-OH; High resolution XPS spectra of (VII) Cd 3d, (VIII) O 1s after the sorption of Cd^{2+} ; and (IX) Cu 2p, by 3-D SGMMCs-(OH)₂.

binding energy of Zr-OH bond moved to lower value from 531.80 eV to 531.75 eV, which clearly showed that uncoordinated Zr-OH bonds provided strong Lewis acid-based interaction for the adsorption of Cd²⁺ on/in the sorbent [33] (Fig. 9(IV)). The Cd²⁺ species can be combined with the hydroxyl group of Zr-O-H bond to form a Zr-O-Cd²⁺ coordination bond, releasing H⁺ and hydroxyl group to form water in the solution, suggesting that hydroxyl groups played a key role in Cd²⁺ adsorption via strong inner-sphere coordination interactions [60,93]. In addition, the binding energy of Zr-O-C peak also moved to lower value from 532.95 eV to 532.52 eV, which clearly suggested the involvement of the BDC-OH aromatic linkers of MOF-NPs in the adsorption of Cd²⁺ via aromatic ligands exchange mechanism [58]. Further, a slight change was also noticed in XPS profile of C 1s after sorption, because the characteristic peak of C-containing groups shifted from 284.80 to 284.87 eV, which indicated the consumption of hydrophilic functional groups (-COOH) during the sorption process. Notably, the binding energy value of Zr-O-C peak moved to lower value from 286.45 eV to 285.85 eV, which also hinted the attachment of Cd²⁺ ions with the BDC aromatic linker of MOF-NPs (Fig. S7(I)).

Similarly, the peaks at around 931.33 and 951.14 eV seemed in the XPS contour of Cu 2p, which can be allocated to the Cu²⁺ binding energies of 2p_{3/2} and 2p_{1/2} detours, respectively [63,94–96]. The deconvolution of Cu 2p_{3/2} spectrum produced two peaks with binding energies of 931.33 and 933.27 eV. The existence of the four satellite peaks at 946.94, 943.63, 941.97 and 940.65 eV, confirming the presence of Cu (II) [97–99]. Further, the two peaks of Cu 2p_{3/2} can respectively be assigned to copper hydroxide and the electron-rich environmental Cu (II) [100–102]. The electron-rich environment was provided by complexation with carboxyl and hydroxyl groups of the membrane capsules, and Cu—O is formed on the adsorption surface during the adsorption reaction [103]. The presence of these peaks ensured that Cu²⁺ particles were effectively adsorbed onto/in the membrane capsules (Fig. 9(V)). Further, the binding energy of oxygen-containing groups in the O 1s shifted from 532.05 to 531.12 eV, which evoked the involvement of hydroxyl/-OH and carboxyl/-COOH groups in the adsorption of Cu²⁺ on/in the sorbent via electrostatic attraction and/or ion-exchange mechanism. Noticeably, the binding energy of Zr—OH bond moved to lower value from 531.80 eV to 531.15 eV, which clearly showed that uncoordinated Zr-OH bonds provided strong Lewis acid-based interaction for the adsorption of Cu²⁺ on/in the sorbent [33] (Fig. 9(VI)). The Cu²⁺ species can be combined with the hydroxyl group of Zr-O-H bond to form a Zr-O-Cu²⁺ coordination bond, releasing H⁺ and hydroxyl group to form water in the solution [93]. In addition, the binding energy of Zr-O-C peak also moved to lower value from 532.95 eV to 532.18 eV, which clearly suggested the involvement of the BDC-OH aromatic linkers of MOF-NPs in the adsorption of Cd²⁺ via aromatic ligands exchange mechanism [58]. The characteristic peak of C=O/C—OH was noticeably shifted from 287.80 to 286.71 eV in the C 1s spectra, suggested the attachment of Cu²⁺ with the carboxyl/-COOH groups of the sorbent via electrostatic attraction and/or ion-exchange mechanism (Fig. S7(II)). Notably, the binding energy value of Zr-O-C peak moved to lower value from 286.45 eV to 284.85 eV, which hinted the attachment of Cu²⁺ with the BDC linker of MOF-NPs [58]. Noticeably, the binding energy of Zr 3d moved to lower values from 182.1 eV to 181.45 and 181.84 eV after the adsorption of Cu²⁺ and Cd²⁺, respectively, which may imply the ligand consumption by interaction with metal ions [61]. In addition, Zr—O bonds played a significant role on the adsorption of metal ions and the adsorption mechanism of Zr—O toward metal ions on membrane capsules might be mainly because of the electrostatic interaction, inner-sphere coordination bonds and ligand exchange [82].

Similarly, in case of 3-D SGMMCs-(OH)₂, two main peaks at around 405.74 and 412.79 eV emerged in the XPS contour of Cd 3d, which can be allocated to the Cd²⁺ binding energy of 3d_{5/2} and 3d_{3/2} deviations, respectively [83–85]. The energy difference was 7.05 eV [86]. The Cd3d_{5/2} and Cd3d_{3/2} characteristic peaks appeared at 406.26 and 413.75 eV, respectively and these peaks can be associated to Cd²⁺-X or

Cd-π bonding supported by C=C [87–89], while the other peaks at 405.63 and 412.79 eV reflected the coordination interaction of Cd²⁺ with the oxygen containing functional groups (—OH, —COOH) of the membrane capsules to form Cd—O bonding [90–92]. The manifestation of these peaks in XPS spectra ensured that Cd²⁺ particles were effectively adsorbed onto/in the membrane capsules [72] (Fig. 9(VII)). Furthermore, the high-resolution spectra of O 1s depicted that the binding energy of oxygen-containing groups changed from 532.07 to 530.19 eV, which ensured the contribution of hydrophilic groups (C=O, —OH and C—O) in the sorption of Cd²⁺ on/in the sorbent via electrostatic attraction and/or ion-exchange mechanism. Noticeably, the binding energy of Zr-OH bond moved to lower value from 531.79 eV to 531.34 eV, which clearly showed that uncoordinated Zr-OH bonds provided strong Lewis acid-based interaction for the adsorption of Cd²⁺ on/in the sorbent [33]. The Cd²⁺ species can be combined with the hydroxyl group of Zr-O-H bond to form a Zr-O-Cd²⁺ coordination bond, releasing H⁺ and hydroxyl group to form water in the solution [93] (Fig. 9(VIII)). In addition, the binding energy of Zr-O-C peak also moved to lower value from 532.62 eV to 532.07 eV, which clearly suggested the involvement of the BDC-OH aromatic linkers of MOF-NPs in the adsorption of Cd²⁺ via aromatic ligands exchange mechanism [58].

A slight change was also noticed in XPS profile of C 1s after sorption, because, the characteristic peak of C-containing groups moved from 284.80 to 284.81 eV, which indicated the consumption of hydrophilic functional groups (-COOH/-OH) during the sorption process (Fig. S7 (III)). Notably, the binding energy value of Zr-O-C peak moved to lower value from 286.07 eV to 285.85 eV, which hinted the attachment of Cd²⁺ with the BDC linker of MOF-NPs [58]. Furthermore, the peaks at around 932.96 and 952.78 eV seemed in the XPS contour of Cu 2p, which can be allocated to the Cu²⁺ binding energies of 2p_{3/2} and 2p_{1/2} detours, respectively [63,94–96]. The deconvolution of Cu 2p_{3/2} spectrum produced two peaks with binding energies of 932.96 and 934.68 eV. The existence of the three satellite peaks at 948.72, 944.55, and 940.03 eV, confirming the presence of Cu (II) [97–99]. Notably, the two peaks of Cu 2p_{3/2} can respectively be assigned to copper hydroxide and the electron-rich environmental Cu (II) [100–102]. The electron-rich environment was provided by complexation with carboxyl and hydroxyl groups of the membrane capsules, and Cu—O is formed on the adsorption surface during the adsorption reaction [103]. The presence of these peaks suggested that Cu²⁺ particles were effectively adsorbed onto/in the 3-D SGMMCs-(OH)₂ (Fig. 9(IX)). Furthermore, the binding energy of oxygen-containing groups in the O 1s shifted from 531.91 to 531.01 eV, which evoked the involvement of hydroxyl/-OH and carboxyl/-COOH groups in the adsorption of Cu²⁺ on/in the sorbent via electrostatic attraction and/or ion-exchange mechanism (Fig. S7(IV)). Noticeably, the binding energy of Zr—OH bond moved to lower value from 531.79 eV to 530.35 eV, which clearly showed that uncoordinated Zr—OH bonds provided strong Lewis acid-based interaction for the adsorption of Cd²⁺ on/in the sorbent [33]. The Cd²⁺ species can be combined with the hydroxyl group of Zr—O—H bond to form a Zr-O-Cd²⁺ coordination bond, releasing H⁺ and hydroxyl group to form water in the solution [93]. In addition, the binding energy of Zr—O—C peak also moved to lower value from 532.62 eV to 531.47 eV, which clearly suggested the involvement of the BDC-OH aromatic linkers of MOF-NPs in the adsorption of Cd²⁺ via aromatic ligands exchange mechanism [58].

The characteristic peak of C=O/C—OH was noticeably shifted from 287.82 to 286.40 eV in the C 1s spectra, which hinted the attachment of Cd²⁺ with the carboxyl/-COOH groups of the sorbent via electrostatic attraction and/or ion-exchange mechanism (Fig. S7(V)). Notably, the binding energy value of Zr-O-C peak moved to lower value from 286.07 eV to 284.90 eV, which hinted the attachment of Cd²⁺ with the BDC linker of MOF-NPs [58]. Further, the binding energy of Zr 3d moved to lower values from 182.03 eV to 181.07 and 181.37 eV after the adsorption of Cu²⁺ and Cd²⁺, respectively, which may imply the ligand consumption by interaction with metal ions [61]. In addition, Zr—O

bonds played a significant role on the adsorption of metal ions and the adsorption mechanism of Zr—O toward metal ions on membrane capsules might be mainly because of the electrostatic interaction, inner-sphere coordination interaction and aromatic ligands exchange [82]. In addition, Table 3 is depicting that the atomic contents of C and O were dropped after the sorption of PTMs, which clearly suggested that the reactive hydrophilic functional groups (-COOH and -OH) were devoted /utilized during the elimination of PTMs by 3-D SGMMCs-OH/(OH)₂. Noticeably, the XPS findings well agreement with FTIR and EDX/S results and confirmed the adsorption of PTMs in the 3-D SGMMCs-OH/(OH)₂. Altogether, the adsorptive mechanism of Cu²⁺ and Cd²⁺ by 3-D SGMMCs-OH/(OH)₂ is mainly related to electrostatic interaction, ion-exchange, inner-sphere coordination bonds/interactions and aromatic ligands exchange mechanisms. All the interactions synergistically promoted the adsorption process of metal ions on/in membrane capsules (Fig. 10).

3.10. Practical application in real electroplating wastewater treatment

Table 4 revealed the experimental results of the treatment of Cu-containing real electroplating wastewater by 3-D SGMMCs-OH/(OH)₂ at pH 6. The findings implied that on average >70 % ejection efficacy of Cu²⁺ was achieved in the incidence of other competitive metal ions and pollutants. Notably, improving the amount of capsules dosage from 1 to 1.5 g, the elimination efficacy was significantly improved. Moreover, the findings indicated that the presence of other competitive metal ions did also inhibit the actual selectivity of Cu²⁺ by 3-D SGMMCs-OH/(OH)₂ under selected experimental conditions. On the other hand, an appreciable reduction in other parameters, like, turbidity, TS, TDS, and EC, was also noticed. However, in some cases, the capsules were unable to reduce the COD concentration from solution, as apparent from Table 4. This might be due to the toxicity nature of metal ions, which directly or indirectly affected on the growth and biochemical activities of the persisted microbial community, resulting in declined dissolved oxygen (DO) level and enhanced the concentration of COD [67]. Noticeably, this increase in COD concentration did not influence the removal of targeted metal ions by 3-D SGMMCs-OH/(OH)₂. Furthermore, the color of the capsules was significantly changed after the treatment of Cu-containing real electroplating plating wastewater (Fig. 10). This color changing was significantly different as compared to the employment of capsules in

single Cu-containing synthetic solution, which clearly hinted the attachment of other competitive metal ions and pollutants in the 3-D SGMMCs-OH/(OH)₂ (Fig. 10). Altogether, the obtained results clearly indicate a great potential of 3-D SGMMCs-OH/(OH)₂ in real electroplating wastewater.

Furthermore, Table 5 shows that our as-developed 3-D SGMMCs-OH/(OH)₂ had reasonably much higher adsorptive capacity to eradicate PTMs from sewage than most of the other utilized sorbents.

4. Some comments and suggestions from the authors of this study

The loading of MOFs particles enhanced the overall adsorption performance of the composite sorbent; however, this technique may eventually affect the surface area of the final sorbent. Thus, future investigations should be focused on this point how we can maintain a better surface area of the final composite sorbent that will not decline the overall adsorption performance of the final sorbent. Further, MOFs loaded membrane capsules may leach metals ions in the aqueous solution at some point during wastewater treatment because real situation is dynamic as compared to laboratory conditions, and this state will eventually harm the stability of the sorbents. Thus, more efforts would be needed in future examinations to optimize fabrication protocol to improve overall stability of the final composite sorbent. Likewise, these membrane capsules can't be applicable under complex environmental conditions since they are highly pH dependent. In this study, the as-fabricated membrane capsules were applicable in the pH range of 5–7 and gave best removal performance at pH 6 because of having their highest negative surface charge at this pH. Thus, fine tuning of membrane capsules' functionalities by using different techniques would make them applicable under complex environmental conditions. Hence, future investigations should be focused in this direction. Furthermore, the disposal of the sorbents is a challenging task nowadays, that was the reason we fabricated membrane capsules by using biodegradable alginate biopolymer. However, during disposal, alginate will automatically biodegrade with the passage of time, but the metal contents will remain as such, and it may eventually generate secondary pollutants in the shape of toxic metals in the environment. Therefore, the best option is to design a strategy to recover metals from exhausted biosorbents and then dispose them in a proper way to completely minimize the generation of

Table 3

High resolution X-ray photoelectron spectroscopy (XPS) analysis of 3-D SGMMCs after the sorption of Cu²⁺ and Cd²⁺ by 3-D SGMMCs-OH and 3-D SGMMCs-(OH)₂.

Region/chemical elements	Assignment/chemical bonding	Before adsorption		3-D SGMMCs-OH			
		Peak Be (eV)	Atomic %	After adsorption of Cu ²⁺		After adsorption of Cd ²⁺	
				Peak Be (eV)	Atomic %	Peak Be (eV)	Atomic %
O 1s	O—Ca, Zr—OH, Zr—O—C	532.05	53.48	531.12	39.41	531.70	38.89
C 1s	C—O, C—OH, C=O, Zr—O—C	284.8	30.77	284.81	55.16	284.87	58.2
Ca 2p	Ca—O	347.02	10.06	—	—	—	—
Zr3d	Zr—O	182.1	3.51	181.45	1.27	181.84	1.57
Na1s	Na—O	1071.03	0.02	—	—	—	—
Cu2p	Cu2p _{3/2} , Cu2p _{1/2}	—	—	931.33	2.65	—	—
Cd3d	Cd3d _{5/2} , Cd 3d _{3/2}	—	—	—	—	404.97	1.34

Region/chemical elements	Assignment/chemical bonding	Before adsorption		3-D SGMMCs-(OH) ₂			
		Peak Be (eV)	Atomic %	After adsorption of Cu ²⁺		After adsorption of Cd ²⁺	
				Peak Be (eV)	Atomic %	Peak Be (eV)	Atomic %
O 1s	O—Ca, Zr—OH, Zr—O—C	531.91	39.94	531.01	40.84	531.31	39.85
C 1s	C—O, C—OH, C=O, Zr—O—C	284.84	55.98	284.81	55.59	284.81	57.31
Ca 2p	Ca—O	346.84	3.31	—	—	346.26	2.05
Zr3d	Zr—O	182.03	0.79	181.07	0.76	181.37	0.47
Na1s	Na—O	1071.05	0.01	—	—	—	—
Cu2p	Cu2p _{3/2} , Cu2p _{1/2}	—	—	932.96	2.78	—	—
Cd3d	Cd3d _{5/2} , Cd 3d _{3/2}	—	—	—	—	405.74	0.31

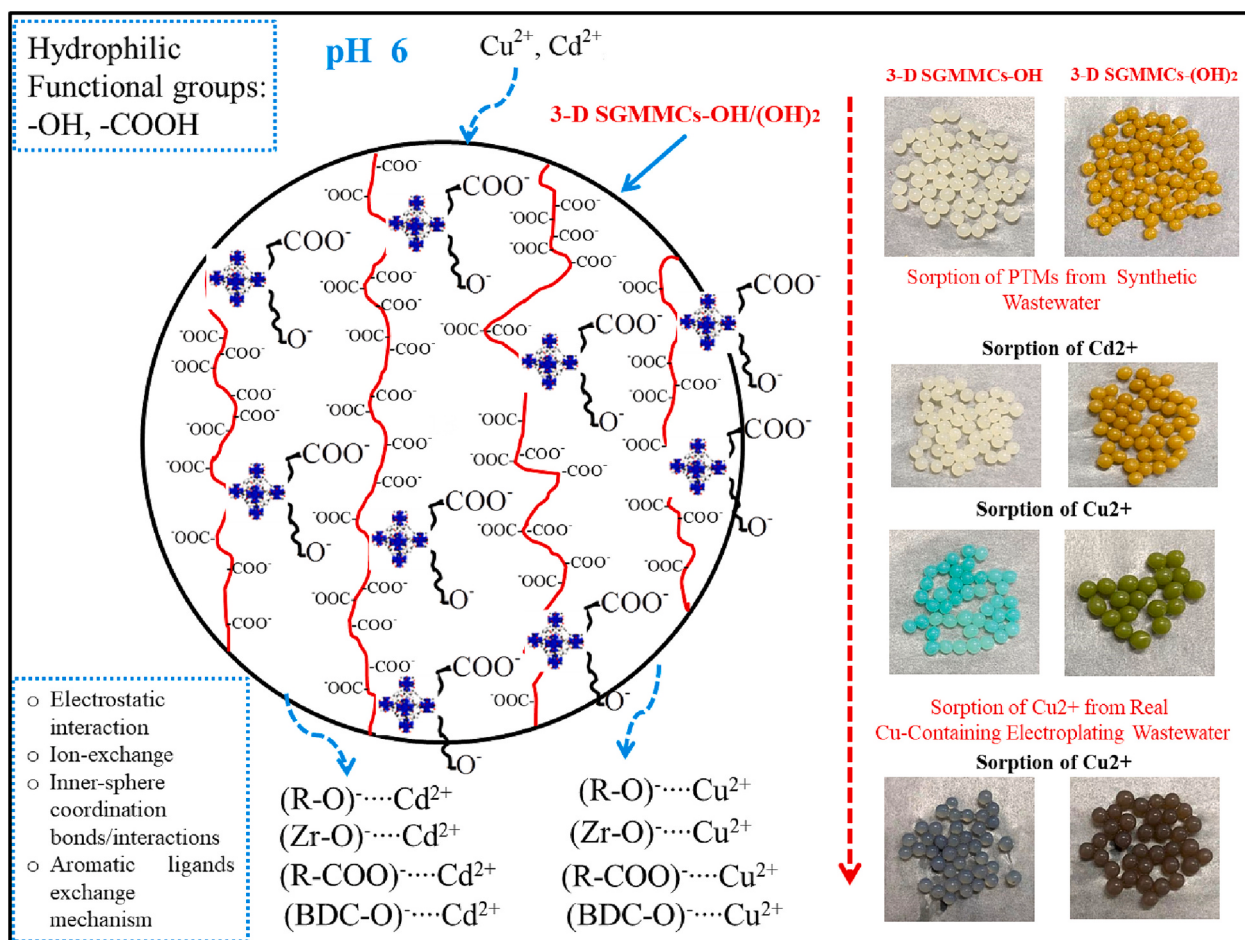


Fig. 10. Proposed adsorptive mechanism/removal mechanism of PTMs (Cu²⁺ and Cd²⁺) by 3-D SGMMCs-OH/(OH)₂ and possible interaction of 3-D SGMMCs-OH/(OH)₂ with PTMs via electrostatic interaction, ion-exchange, inner-sphere coordination bonds/interactions, and aromatic ligands exchange mechanism to adsorb PTMs in the pH range of 1–8 [inset photos are the real representation of the as-prepared capsules before and after the sorption of PTMs from synthetic and real Cu-containing electroplating wastewater].

secondary pollutants for achieving zero-effluent discharge concept.

5. Conclusions

Altogether, the novel mixed matrix 3-D MCs containing UiO-66-OH and UiO-66-(OH)₂ MOF-NPs were developed using sodium alginate (SA) biopolymer via a simple and facile approach to eradicate Cu²⁺ and Cd²⁺ metal ions from water and real electroplating effluent. The findings of FTIR, XRD, XPS, EDX and SEM confirmed the successful loading of MOF-NPs into 3-D MCs. In addition, the pH study and XPS results revealed that the hydrophilic functional groups (-OH and -COOH) played an important role in the smooth loading of MOF-NPs into capsules via intra/inter-molecular hydrogen bonding and van der Waals forces under the selected conditions. SEM results revealed that the 3-D SGMMCs-OH/(OH)₂ had honeycomb porous configuration, which occupied top dense, porous screen mesh, undulated and rough channel like architecture. Further, the MOF crystals were spotted from the outer shell to interior crux of the capsules, which hinted the homogenous distribution of MOF-NPs in/on the as-synthesized 3-D SGMMCs-OH/(OH)₂. Moreover, the maximum monolayer uptake capacities of Cd²⁺ and Cu²⁺ by 3-D SGMMCs-OH were 940 and 1150 mg/g, respectively, and by 3-D SGMMCs-(OH)₂ were 1375 and 1575 mg/g, respectively, under optimum conditions. The manifestation of pendant functional groups (-COOH and -OH) competed a critical responsibility in eradicating PTMs. Further, the Langmuir and Pseudo-second order models fitted well with the sorption data. In addition, the isotherms, kinetics,

thermodynamic, FTIR, EDX and XPS findings implied that adsorption was exothermic, and electrostatic interaction and ion-exchange were the key eradication mechanism owing to the demonstration of plentiful reactive -COOH and -OH groups on/in the capsules. Notably, Zr-OH and BDC-OH/(OH)₂ aromatic linkers played vital roles in Cu²⁺ and Cd²⁺ adsorption by participating in inner-sphere coordination interactions and aromatic ligands exchange mechanisms, as ensured via FTIR and XPS techniques. In addition, the sorbent depicted superior selectivity against targeted metal cations under designated conditions and maintained >80 % eradication efficiency upto six (06) repeated cycles. The material depicted good performance in removing targeted metal cations from real electroplating wastewater and achieved >70 % removal efficiency of Cu²⁺ in the incidence of other competitive metal ions and pollutants. Therefore, the as-developed 3-D SGMMCs-OH/(OH)₂ depicted a comparatively maximum sorption performance to eradicate targeted metal cations from water and real electroplating wastewater. Thus, such kind of MOF-based 3-D capsules is highly a prerequisite to remove and recover PTMs from industrial wastewaters in the future.

CRediT authorship contribution statement

Imran Ali: Writing – original draft, Visualization, Validation, Methodology, Investigation, Formal analysis, Data curation, Conceptualization. **Changsheng Peng:** Investigation. **Xiao Tan:** Writing – review & editing. **Huibin Sun:** Methodology. **Juying Li:** Writing – review & editing, Writing – original draft, Visualization, Investigation, Funding

Table 4

Treatment of copper-containing real electroplating wastewater by the as-prepared 3-D SGMMCs-OH and 3-D SGMMCs-(OH)₂ at two different dosages (X₁: 1 g and X₂: 1.5 g) [V: 50 mL; pH: 6; contact time: 100 h; shaking speed: 130 rpm; temperature: 298.15 K].

Physico-chemical characteristics	Factory															
	A				B				C				D			
	C ₀	X ₁	X ₂	X ₁ -X ₂	C ₀	X ₁	X ₂	X ₁ -X ₂	C ₀	X ₁	X ₂	X ₁ -X ₂	C ₀	X ₁	X ₂	X ₁ -X ₂
3-D SGMMCs-OH																
Turbidity (NTU)	33	3.2	2.90	90–91	38	3.58	2.95	90–92	28	2.13	1.29	92–95	24	1.57	1.02	93–95
TS (g/L)	49	39	32	20–34	37	30	23	18–37	42	36	28	14–33	52	35	30	32–42
TDS (g/L)	>35 (~43)	31	28	28–35	34	24	18	29–47	>35 (~38)	30	27	21–29	>35 (~48)	33	28	31–41
EC (µs/cm)	>50 (~71)	22	19	69–73	>50 (~68)	16	12	76–82	>50 (~83)	19	15	77–82	>50 (~68)	14	8	79–88
COD (mg/L)	933	468	452	50–51	571	653	670	-(14–17)	143	33	28	77–80	98	267	273	-(63–64)
TCr (mg/L)	0.214	0.122	0.110	43–48	124.85	107.86	99.89	13–20	150.21	142.3	133.8	5–11	0.240	ND	ND	100
Cr(VI) (mg/L)	0.210	0.132	0.120	37–43	123.54	109.7	98.23	11–20	149.26	138.65	130.21	7–13	0.238	ND	ND	100
Cr ³⁺ (mg/L)	0.004	ND	ND	100	1.31	ND	ND	100	0.95	ND	ND	100	0.002	ND	ND	100
Cu ²⁺ (mg/L)	12.63	5.040	0.95	60–92	106.04	42.3	15.2	60–86	109.23	44.036	12.56	59–88	1.085	0.961	ND	11–100
Cd ²⁺ (mg/L)	ND	ND	ND	–												
Zn ²⁺ (mg/L)	10.95	0.99	0.12	91–99	1.61	0.633	0.1	60–93	ND	ND	ND	–	ND	ND	ND	–
Mg ²⁺ (mg/L)	4.51	3.697	1.13	18–75	6.132	4.28	2.30	30–62	5.1	1.95	0.42	62–92	1.892	0.6558	0.19	65–90
Na ⁺ (mg/L)	1120.1064	411.82	206.5	63–81	820.64	338.93	198.5	59–76	365.21	154.33	78.5	58–78	107.07	31.72	18.9	70–82
3-D SGMMCs-(OH)₂																
Turbidity (NTU)	33	3.12	2.75	90–92	38	3.12	2.65	92–93	28	2.10	1.83	92–93	24	1.84	0.58	92–97
TS (g/L)	49	31	28	37–43	37	26	18	30–51	42	30	22	28–47	52	33	28	36–46
TDS (g/L)	>35 (~43)	29	25	32–41	34	23	17	32–50	>35 (~38)	28	21	26–45	>35 (~48)	31	26	35–45
EC (µs/cm)	>50 (~71)	20	18	71–75	>50 (~68)	15	11	78–84	>50 (~83)	18	16	78–81	>50 (~68)	15	9	78–86
COD (mg/L)	933	539	510	42–45	571	571	570	0–0.17	143	352	361	-(59–60)	98	239	242	-(59–60)
TCr (mg/L)	0.214	0.082	0.041	61–81	124.85	62.90	42.89	50–66	150.21	21.085	19.85	85–87	0.240	ND	ND	100
Cr(VI) (mg/L)	0.210	0.092	0.058	56–72	123.54	62.28	42.12	49–65	149.26	21.01	19.80	85–86	0.238	ND	ND	100
Cr ³⁺ (mg/L)	0.004	ND	ND	100	1.31	ND	ND	100	0.95	ND	ND	100	0.002	ND	ND	100
Cu ²⁺ (mg/L)	12.63	3.50	0.20	72–98	106.04	36.49	11.25	65–90	109.23	39.65	9.85	64–91	1.085	0.829	ND	24–100
Cd ²⁺ (mg/L)	ND	ND	ND	–												
Zn ²⁺ (mg/L)	10.95	1.42	0.95	87–91	1.61	1.12	1.02	30–37	ND	ND	ND	–	ND	ND	ND	–
Mg ²⁺ (mg/L)	4.51	1.42	1.13	68–75	6.132	5.23	2.13	15–65	5.1	1.87	0.59	63–88	1.892	ND	ND	100
Na ⁺ (mg/L)	1120.1064	1.420	1.02	99–99.5	820.64	26.500	15.23	97–98	365.21	1.871	1.13	99–99.4	107.07	ND	ND	100

Key: TS: Total Solid; TDS: Total dissolved solid; EC: Electrical Conductivity; COD: Chemical Oxygen Demand; TCr: Total Cr; ND: Not detected; –: cannot measure; –O: reduction in removal efficiency; C₀: Initial pollutant concentration; C_{eq}: Final concentration at equilibrium; R.E: Removal efficiency (%)

Table 5

Comparison of 3-D SGMMCs-OH and 3-D SGMMCs-(OH)₂ with other employed sorbents for the adsorptive removal of potentially toxic metals, (i.e., Cd²⁺ and Cu²⁺) from wastewater.

Sorbent	q _e (mg/g)	Reference(s)
Cd²⁺		
Residue of <i>Padina gymnospora</i> (RPG)	99.85	[104]
Commercial resin of Duolite GT-73	105.7	[69]
Poly(methacrylic acid)grafted chitosan microspheres	146.1	[105]
Chelated polyacrylonitrile beads	156	[78]
PSSA-AC	184.12	[77]
Liquid-core gellan-alginate capsules	197	[75]
PEO/chitosan nanofiber	248.1	[106]
Poly(itaconic acid) grafted chitosan with glutaraldehyde cross-linking	405	[107]
PAN/chitosan/UiO-66-NH ₂ nanofibers	415.6	[108]
Bio-magnetic membrane capsules (BMMCs)	610.67	[72]
Aminated PAN/chitosan/ rectorite fibers	714	[109]
3-D SGMMCs-OH	940	Present study
3-D SGMMCs-(OH)₂	1375	Present study
Cu²⁺		
EDA-SAMMS	26	[110]
Mullite Whiskers/Cordierite Porous Ceramics	54.94	[111]
Polyaniline/calcium alginate composite	79.0	[112]
Mxene/alginate composites	87.6	[79]
Calcium alginate/graphene oxide composite aerogel	98.1	[113]
Carboxymethylated CNFs (CMCNFs)	115.3	[114]
Liquid-core gellan-alginate capsules	219	[75]
3-D SGMMCs-OH	1150	Present study
3-D SGMMCs-(OH)₂	1575	Present study

acquisition, Formal analysis, Conceptualization.

Declaration of competing interest

The authors declare no conflict of interest.

Data availability

The authors do not have permission to share data.

Acknowledgment

This study was financially supported by National Natural Science Foundation of China (No. 21777104, 52250410354), and the Science and Technology Planning Project of Shenzhen Municipality (No. JCYJ20190808152817031). This research was also funded by the Jiangsu Province Postdoctoral Excellence Program (2022ZB154).

Appendix A. Supplementary data

Supplementary data to this article can be found online at <https://doi.org/10.1016/j.ijbiomac.2024.131312>.

References

- [1] N. Abdollahi, G. Moussavi, S. Giannakis, A review of heavy metals' removal from aqueous matrices by metal-organic frameworks (MOFs): state-of-the art and recent advances. *Journal of environmental, Chem. Eng.* 10 (3) (June 2022) 107394.
- [2] L. Fu, S. Wang, G. Lin, L. Zhang, Q. Liu, H. Zhou, et al., Post-modification of UiO-66-NH₂ by resorcylic aldehyde for selective removal of Pb (II) in aqueous media, *J. Clean. Prod.* 229 (2019) 470–479.
- [3] Y. Guo, H. Lu, F. Zhao, X. Zhou, W. Shi, G. Yu, Biomass-derived hybrid hydrogel evaporators for cost-effective solar water purification, *Adv. Mater.* 32 (2020) 1907061.
- [4] Y. Jiang, F. Yang, M. Dai, I. Ali, X. Shen, X. Hou, et al., Application of microbial immobilization technology for remediation of Cr (VI) contamination: a review, *Chemosphere* 131721 (2021).
- [5] X. Zhao, X. Yu, X. Wang, S. Lai, Y. Sun, D. Yang, Recent advances in metal-organic frameworks for the removal of heavy metal oxoanions from water, *Chem. Eng. J.* 127221 (2020).
- [6] I. Ali, C. Peng, Z.M. Khan, I. Naz, M. Sultan, M. Ali, et al., Overview of microbes based fabricated biogenic nanoparticles for water and wastewater treatment, *J. Environ. Manage.* 230 (2019) 128–150.
- [7] M. He, L. Wang, Z. Zhang, Y. Zhang, J. Zhu, X. Wang, et al., Stable forward osmosis nanocomposite membrane doped with sulfonated graphene oxide@ metal-organic frameworks for heavy metal removal, *ACS Appl. Mater. Interfaces* 12 (51) (2020) 57102–57116.
- [8] M.E. Mahmoud, A.K. Mohamed, Novel derived pectin hydrogel from mandarin peel based metal-organic frameworks composite for enhanced Cr (VI) and Pb (II) ions removal, *Int. J. Biol. Macromol.* 164 (2020) 920–931.
- [9] L. Esrafilii, F.D. Firuzabadi, A. Morsali, M.-L. Hu, Reuse of predesigned dual-functional metal organic frameworks (DF-MOFs) after heavy metal removal, *J. Hazard. Mater.* 403 (2021) 123696.
- [10] Y. Zhang, M. Dai, K. Liu, C. Peng, Y. Du, Q. Chang, et al., Appraisal of Cu (II) adsorption by graphene oxide and its modelling via artificial neural network, *RSC Adv.* 9 (2019) 30240–30248.
- [11] I. Ali, J. Li, C. Peng, M. Qasim, Z.M. Khan, I. Naz, et al., 3-dimensional membrane capsules: synthesis modulations for the remediation of environmental pollutants—a critical review, *Crit. Rev. Environ. Sci. Technol.* (2020) 1–62.
- [12] Y. Du, M. Dai, I. Naz, X. Hao, X. Wei, R. Rong, et al., Carbothermal reduction synthesis of zero-valent iron and its application as a persulfate activator for ciprofloxacin degradation, *Sep. Purif. Technol.* 275 (2021) 119201.
- [13] Y. Fang, X. Wu, M. Dai, A. Lopez-Valdivieso, S. Raza, I. Ali, et al., The sequestration of aqueous Cr (VI) by zero valent iron-based materials: from synthesis to practical application, *J. Clean. Prod.* 127678 (2021).
- [14] M.I. Hossain, A. Udo, B.E. Grabicka, K.S. Walton, S.M. Ritchie, T.G. Glover, Membrane-coated UiO-66 MOF adsorbents, *Industrial & Engineering Chemistry Research* 58 (2018) 1352–1362.
- [15] S. Raza, J. Zhang, I. Ali, X. Li, C. Liu, Recent trends in the development of biomass-based polymers from renewable resources and their environmental applications, *J. Taiwan Inst. Chem. Eng.* 115 (October 2020) 293–303.
- [16] S. Raza, J. Zhang, I. Ali, X. Li, C. Liu, Recent trends in the development of biomass-based polymers from renewable resources and their environmental applications, *J. Taiwan Inst. Chem. Eng.* 115 (2020) 293–303.
- [17] S.A. Younis, E.E. Kwon, M. Qasim, K.-H. Kim, T. Kim, D. Kukkar, et al., Metal-organic framework as a photocatalyst: progress in modulation strategies and environmental/energy applications, *Prog. Energy Combust. Sci.* 81 (2020) 100870.
- [18] X. Tan, W. Gao, Z. Duan, N. Zhu, X. Wu, I. Ali, Y. Ruan, Synthesis of novel algal extracellular polymeric substances (EPS)-based hydrogels for the efficient removal and recovery of phosphorus from contaminated waters: development, characterisation, and performance, *J. Environ. Chem. Eng.* 11 (2023) 109044.
- [19] K. Wang, J. Wu, M. Zhu, Y.-Z. Zheng, X. Tao, Highly effective pH-universal removal of tetracycline hydrochloride antibiotics by UiO-66(COOH) 2/GO metal-organic framework composites, *J. Solid State Chem.* 284 (2020) 121200.
- [20] G.-R. Xu, Z.-H. An, K. Xu, Q. Liu, R. Das, H.-L. Zhao, Metal organic framework (MOF)-based micro/nanoscaled materials for heavy metal ions removal: the cutting-edge study on designs, synthesis, and applications, *Coord. Chem. Rev.* 427 (2021) 213554.
- [21] I. Zawierucha, C. Kozlowski, G. Malina, Immobilized materials for removal of toxic metal ions from surface/groundwaters and aqueous waste streams, *Environ. Sci.: Processes Impacts* 18 (2016) 429–444.
- [22] C. Xiong, S. Wang, P. Hu, L. Huang, C. Xue, Z. Yang, et al., Efficient selective removal of Pb (II) by using 6-aminothiouracil-modified Zr-based organic frameworks: from experiments to mechanisms, *ACS Appl. Mater. Interfaces* 12 (2020) 7162–7178.
- [23] G. Yuan, Y. Tian, M. Li, Y. Zeng, H. Tu, J. Liao, et al., Removal of Co (II) from aqueous solution with functionalized metal-organic frameworks (MOFs) composite, *J. Radioanal. Nucl. Chem.* 322 (2019) 827–838.
- [24] S. Chen, J. Liu, Y. Xu, Z. Li, T. Wang, J. Xu, Z. Wang, Hydrogen storage properties of the novel crosslinked UiO-66-(OH) 2, *Int. J. Hydrogen Energy* 43 (2018) 15370–15377.
- [25] Y. Peng, H. Huang, Y. Zhang, C. Kang, S. Chen, L. Song, et al., A versatile MOF-based trap for heavy metal ion capture and dispersion, *Nat. Commun.* 9 (2018) 1–9.
- [26] L. Zhang, Z. Yan, X. Chen, M. Yu, F. Liu, F. Cheng, J. Chen, Facile synthesis of amorphous MoS x-Fe anchored on Zr-MOFs towards efficient and stable electrocatalytic hydrogen evolution, *Chem. Commun.* 56 (2020) 2763–2766.
- [27] X. Gao, R. Ding, H. Huang, B. Liu, X. Zhao, Constructing a carboxyl-rich angstrom-level trap in a metal-organic framework for the selective capture of lithium, *Chem. Commun.* 59 (2023) 13183–13186.
- [28] X. Gao, B. Liu, X. Zhao, Thiol-decorated defective metal-organic framework for effective removal of mercury (II) ion, *Chemosphere* 317 (2023) 137891.
- [29] P.A. Kobielska, A.J. Howarth, O.K. Farha, S. Nayak, Metal-organic frameworks for heavy metal removal from water, *Coord. Chem. Rev.* 358 (2018) 92–107.
- [30] D. Roy, S. Neogi, S. De, Adsorptive removal of heavy metals from battery industry effluent using MOF incorporated polymeric beads: a combined experimental and modeling approach, *J. Hazard. Mater.* 403 (2021) 123624.

- [31] E.A.A. ElHussein, S. Şahin, S.S. Bayazit, Removal of carbamazepine using UiO-66 and UiO-66/graphene nanoplatelet composite, *J. Environ. Chem. Eng.* 8 (2020) 103898.
- [32] Ü. Kökçam-Demir, A. Goldman, L. Esrafilo, M. Gharib, A. Morsali, O. Weingart, C. Janiak, Coordinatively unsaturated metal sites (open metal sites) in metal–organic frameworks: design and applications, *Chem. Soc. Rev.* 49 (2020) 2751–2798.
- [33] Z. Luo, H. Chen, S. Wu, C. Yang, J. Cheng, Enhanced removal of bisphenol A from aqueous solution by aluminum-based MOF/sodium alginate-chitosan composite beads, *Chemosphere* 237 (2019) 124493.
- [34] J. Nie, H. Xie, M. Zhang, J. Liang, S. Nie, W. Han, Effective and facile fabrication of MOFs/cellulose composite paper for air hazards removal by virtue of in situ synthesis of MOFs/chitosan hydrogel, *Carbohydr. Polym.* 250 (2020) 116955.
- [35] X. Tan, L. Yi, Z. Duan, X. Wu, I. Ali, L. Gao, Phosphorus recovery from wastewater using extracellular polymeric substances (EPS)-like hydrogels, *Journal of Water Process Engineering* 52 (2023) 103512.
- [36] J. Li, X. Wang, G. Zhao, C. Chen, Z. Chai, A. Alsaedi, et al., Metal–organic framework-based materials: superior adsorbents for the capture of toxic and radioactive metal ions, *Chem. Soc. Rev.* 47 (2018) 2322–2356.
- [37] I.A. Kumar, N. Viswanathan, Micro-encapsulation and hydrothermal tuning of amine decorated alginate hybrid beads for nitrate and phosphate remediation, *J. Taiwan Inst. Chem. Eng.* 102 (2019) 283–296.
- [38] I. Ali, J. Li, C. Peng, M. Qasim, Z.M. Khan, I. Naz, et al., 3-Dimensional membrane capsules: synthesis modulations for the remediation of environmental pollutants—a critical review, *Crit. Rev. Environ. Sci. Technol.* 52 (2022) 1092–1153.
- [39] I. Aswin Kumar, H.A. El-Serehy, F.A. Al-Misned, N. Viswanathan, Complex fabrication of Zr^{4+} , La^{3+} , and Ce^{3+} coordinated alginate-assisted bentonite-based hybrid beads for nitrate removal, *J. Chem. Eng. Data* 66 (2021) 979–989.
- [40] Z. Hu, Z. Kang, Y. Qian, Y. Peng, X. Wang, C. Chi, D. Zhao, Mixed matrix membranes containing UiO-66 ($Hf(OH)_2$) 2 metal–organic framework nanoparticles for efficient H_2/CO_2 separation, *Ind. Eng. Chem. Res.* 55 (2016) 7933–7940.
- [41] Z.S. Moghaddam, M. Kaykhaii, M. Khajeh, A.R. Oveisi, Synthesis of UiO-66-OH zirconium metal–organic framework and its application for selective extraction and trace determination of thorium in water samples by spectrophotometry, *Spectrochim. Acta A Mol. Biomol. Spectrosc.* 194 (2018) 76–82.
- [42] Y. Sun, M. Chen, H. Liu, Y. Zhu, D. Wang, M. Yan, Adsorptive removal of dye and antibiotic from water with functionalized zirconium-based metal organic framework and graphene oxide composite nanomaterial Uio-66-(OH) 2/GO, *Appl. Surf. Sci.* 525 (2020) 146614.
- [43] Q. Zhang, Y. Wu, X. Hong, Z. Li, Y. Lei, R. Yu, et al., Different ligand functionalized bimetallic (Zr/Ce) UiO-66 as a support for immobilization of phosphotungstic acid with enhanced activity for the esterification of fatty acids, *Sustain. Chem. Pharm.* 37 (2024) 101344.
- [44] F. Xiao, M. Cao, Y. Chen, UiO-66-(OH) 2-mediated transition layer for ultra-thin homogeneous defect-free polyamide membrane, *Surfaces and Interfaces* 44 (2024) 103607.
- [45] Z. Yang, Y. Ying, Y. Pu, D. Wang, H. Yang, D. Zhao, Poly (ionic liquid)-functionalized UiO-66-(OH) 2: improved interfacial compatibility and separation ability in mixed matrix membranes for CO_2 separation, *Industrial & Engineering Chemistry Research* 61 (2022) 7626–7633.
- [46] T. Li, Z. Zhang, Z. Yang, Encapsulation of phosphotungstic acid into UiO-66-(OH) 2 for synergistic and rapid photocatalytic degradation of organic pollutants, *Mater. Lett.* 134699 (2023).
- [47] Y. Lei, J. Zhao, H. Song, F. Yang, L. Shen, L. Zhu, et al., Enhanced adsorption of dyes by functionalized UiO-66 nanoparticles: adsorption properties and mechanisms, *J. Mol. Struct.* 1292 (2023) 136111.
- [48] L. Zhai, X. Zheng, M. Liu, X. Wang, W. Li, X. Zhu, et al., Tuning surface functionalizations of UiO-66 towards high adsorption capacity and selectivity eliminations for heavy metal ions, *Inorg. Chem. Commun.* 110937 (2023).
- [49] M.M. Abdelnaby, I.M. Tayeb, A.M. Alloosh, H.A. Alyossef, A. Alnoaimi, M. Zeama, et al., Post-synthetic modification of UiO-66 analogue metal–organic framework as potential solid sorbent for direct air capture, *Journal of CO₂ Utilization* 79 (2024) 102647.
- [50] Z. Qiu, M. Zhou, K. Wang, D. Fan, C. Wen, Z. Zhu, et al., Synthesis, characterization, and CO_2 adsorption performance of UiO-66-(OH) 2/GO composite, *Process Saf. Environ. Prot.* 182 (2024) 939–947.
- [51] M.J. Katz, Z.J. Brown, Y.J. Colón, P.W. Siu, K.A. Scheidt, R.Q. Snurr, et al., A facile synthesis of UiO-66, UiO-67 and their derivatives, *Chem. Commun.* 49 (2013) 9449–9451.
- [52] C.H. Sharp, J. Abelard, A.M. Plonka, W. Guo, C.L. Hill, J.R. Morris, Alkane–OH hydrogen bond formation and diffusion energetics of n-butane within UiO-66, *J. Phys. Chem. C* 121 (2017) 8902–8906.
- [53] Z.H. Rada, H.R. Abid, J. Shang, H. Sun, Y. He, P. Webley, et al., Functionalized UiO-66 by single and binary (OH) 2 and NO₂ groups for uptake of CO_2 and CH_4 , *Industrial & Engineering Chemistry Research* 55 (2016) 7924–7932.
- [54] W. Zhu, J. Guo, J.O. Agola, J.G. Croissant, Z. Wang, J. Shang, et al., Metal–organic framework nanoparticle-assisted cryopreservation of red blood cells, *J. Am. Chem. Soc.* 141 (2019) 7789–7796.
- [55] T.K. Vo, V.C. Nguyen, D.T. Quang, B.J. Park, J. Kim, Formation of structural defects within UiO-66 (Zr)-(OH) 2 framework for enhanced CO_2 adsorption using a microwave-assisted continuous-flow tubular reactor, *Microporous Mesoporous Mater.* 312 (2021) 110746.
- [56] K. Fu, Y. Zhang, H. Liu, C. Lv, J. Guo, J. Luo, et al., Construction of metal–organic framework/polymer beads for efficient lead ions removal from water: experiment studies and full-scale performance prediction, *Chemosphere* 303 (2022) 135084.
- [57] S. Yang, L. Peng, O.A. Syzgantseva, O. Trukhina, I. Kochetygov, A. Justin, et al., Preparation of highly porous metal–organic framework beads for metal extraction from liquid streams, *J. Am. Chem. Soc.* 142 (2020) 13415–13425.
- [58] A. Kumar, C. Sharma, UiO-66-NH₂: a recyclable and efficient sorbent for dispersive solid-phase extraction of fluorinated aromatic carboxylic acids from aqueous matrices, *Anal. Bioanal. Chem.* (2023) 1–14.
- [59] Y. Wang, L. Li, P. Dai, L. Yan, L. Cao, X. Gu, X. Zhao, Missing-node directed synthesis of hierarchical pores on a zirconium metal–organic framework with tunable porosity and enhanced surface acidity via a microdroplet flow reaction, *J. Mater. Chem. A* 5 (2017) 22372–22379.
- [60] X. Chen, L. Li, L. Zeng, Y. Wang, T. Zhang, New insight into the co-removal of arsenic and cadmium from wastewater by using thiol-functionalized UiO-66: a mechanistic study and real water test, *Sep. Purif. Technol.* 332 (2024) 125876.
- [61] R. Luo, K. Zhang, Y. Qin, L. Xie, X. Chai, L. Zhang, et al., Amine-functionalized UiO-66 incorporated electrospun cellulose/chitosan porous nanofibrous membranes for removing copper ions, *Chem. Eng. J.* 480 (2024) 148077.
- [62] M. Zhu, X. Huang, Y. Zhu, H. Zhang, S. Lu, Construction of $AgVO_3/UiO-66$ heterojunction for enhanced degradation of tetracycline, *Chemical Physics Impact* 7 (2023) 100333.
- [63] M.R. Awual, M.M. Hasan, A. Islam, A.M. Asiri, M.M. Rahman, Optimization of an innovative composited material for effective monitoring and removal of cobalt (II) from wastewater, *J. Mol. Liq.* 298 (2020) 112035.
- [64] M.R. Awual, A facile composite material for enhanced cadmium (II) ion capturing from wastewater, *J. Environ. Chem. Eng.* 7 (2019) 103378.
- [65] M.R. Karim, M.O. Ajiaz, N.H. Alharbi, H.F. Alharbi, F.S. Al-Mubaddel, M. R. Awual, Composite nanofibers membranes of poly (vinyl alcohol)/chitosan for selective lead (II) and cadmium (II) ions removal from wastewater, *Ecotoxicol. Environ. Saf.* 169 (2019) 479–486.
- [66] M.R. Awual, New type mesoporous conjugate material for selective optical copper (II) ions monitoring & removal from polluted waters, *Chem. Eng. J.* 307 (2017) 85–94.
- [67] M.R. Awual, M.M. Hasan, M.A. Khaleque, M.C. Sheikh, Treatment of copper (II) containing wastewater by a newly developed ligand based facial conjugate materials, *Chem. Eng. J.* 288 (2016) 368–376.
- [68] M.R. Awual, M. Khrasheh, N.H. Alharthi, M. Luqman, A. Islam, M.R. Karim, et al., Efficient detection and adsorption of cadmium (II) ions using innovative nano-composite materials, *Chem. Eng. J.* 343 (2018) 118–127.
- [69] T. Vaughan, C.W. Seo, W.E. Marshall, Removal of selected metal ions from aqueous solution using modified corncobs, *Bioresour. Technol.* 78 (2001) 133–139.
- [70] I. Ali, C. Peng, I. Naz, D. Lin, D.P. Saroj, M. Ali, Development and application of novel bio-magnetic membrane capsules for the removal of the cationic dye malachite green in wastewater treatment, *RSC Adv.* 9 (2019) 3625–3646.
- [71] M.R. Awual, M.M. Hasan, J. Iqbal, A. Islam, M.A. Islam, A.M. Asiri, M. M. Rahman, Naked-eye lead (II) capturing from contaminated water using innovative large-pore facial composite materials, *Microchem. J.* 154 (2020) 104585.
- [72] I. Ali, C. Peng, D. Lin, D.P. Saroj, I. Naz, Z.M. Khan, et al., Encapsulated green magnetic nanoparticles for the removal of toxic Pb^{2+} and Cd^{2+} from water: development, characterization and application, *J. Environ. Manage.* 234 (2019) 273–289.
- [73] M.R. Awual, M.M. Hasan, J. Iqbal, M.A. Islam, A. Islam, S. Khandaker, et al., Ligand based sustainable composite material for sensitive nickel (II) capturing in aqueous media, *J. Environ. Chem. Eng.* 8 (2020) 103591.
- [74] S. Khandaker, Y. Toyohara, G.C. Saha, M.R. Awual, T. Kubo, Development of synthetic zeolites from bio-slag for cesium adsorption: kinetic, isotherm and thermodynamic studies, *Journal of Water Process Engineering* 33 (2020) 101055.
- [75] A. Nussinovich, O. Dagan, Hydrocolloid liquid-core capsules for the removal of heavy-metal cations from water, *J. Hazard. Mater.* 299 (2015) 122–131.
- [76] S. Raza, E. Ghasali, A. Hayat, P. Zhang, Y. Orooji, H. Lin, Sodium alginate hydrogel-encapsulated trans-anethole based polymer: synthesis and applications as an eradicator of metals and dyes from wastewater, *Int. J. Biol. Macromol.* 254 (2024) 127153.
- [77] W. Wei, J.K. Bediako, S. Kim, Y.-S. Yun, Removal of Cd (II) by poly (styrenesulfonic acid)-impregnated alginate capsule, *J. Taiwan Inst. Chem. Eng.* 61 (2016) 188–195.
- [78] P. Bhunia, S. Chatterjee, P. Rudra, S. De, Chelating polyacrylonitrile beads for removal of lead and cadmium from wastewater, *Sep. Purif. Technol.* 193 (2018) 202–213.
- [79] Y. Dong, D. Sang, C. He, X. Sheng, L. Lei, Mxene/alginate composites for lead and copper ion removal from aqueous solutions, *RSC Adv.* 9 (2019) 29015–29022.
- [80] P. Zhang, S. Raza, Y. Cheng, U. Claudine, A. Hayat, T. Bashir, et al., Fabrication of maleic anhydride-acrylamide copolymer based sodium alginate hydrogel for elimination of metals ions and dyes contaminants from polluted water, *Int. J. Biol. Macromol.* 129146 (2024).
- [81] C. Wang, X. Liu, J.P. Chen, K. Li, Superior removal of arsenic from water with zirconium metal–organic framework UiO-66, *Sci. Rep.* 5 (2015) 16613.
- [82] X. Fang, S. Wu, Y. Wu, W. Yang, Y. Li, J. He, et al., High-efficiency adsorption of norfloxacin using octahedral UIO-66-NH₂ nanomaterials: dynamics, thermodynamics, and mechanisms, *Appl. Surf. Sci.* 518 (2020) 146226.
- [83] W. Kong, Q. Yue, Q. Li, B. Gao, Adsorption of Cd^{2+} on GO/PAA hydrogel and preliminary recycle to GO/PAA-CdS as efficient photocatalyst, *Sci. Total Environ.* 668 (2019) 1165–1174.

- [84] F. Wang, J. Li, Y. Su, Q. Li, B. Gao, Q. Yue, W. Zhou, Adsorption and recycling of Cd (II) from wastewater using straw cellulose hydrogel beads, *J. Ind. Eng. Chem.* 80 (2019) 361–369.
- [85] Z. Yang, T. Yang, Y. Yang, X. Yi, X. Hao, T. Xie, C.J. Liao, The behavior and mechanism of the adsorption of Pb (II) and Cd (II) by a porous double network porous hydrogel derived from peanut shells, *Materials Today Communications* 27 (2021) 102449.
- [86] J. Li, M. Chen, X. Yang, L. Zhang, Preparation of a novel hydrogel of sodium alginate using rural waste bone meal for efficient adsorption of heavy metals cadmium ion, *Sci. Total Environ.* 863 (2023) 160969.
- [87] W. Chen, H. Xie, N. Jiang, X. Guo, Z. Liu, Synthesis of magnetic sodium lignosulfonate hydrogel (Fe3O4@ LS) and its adsorption behavior for Cd²⁺ in wastewater, *Int. J. Biol. Macromol.* 125498 (2023).
- [88] W. Ding, H. Liang, H. Zhang, H. Sun, Z. Geng, C. Xu, A cellulose/bentonite grafted polyacrylic acid hydrogel for highly-efficient removal of cd (II), *Journal of Water Process Engineering* 51 (2023) 103414.
- [89] P. Zhang, L. Yuan, J. Zeng, K. Zou, B. Liu, T. Qing, B. Feng, Alginate production of *Pseudomonas* strains and its application in preparation of alginate-biomass hydrogel for heavy metal adsorption, *Int. J. Biol. Macromol.* 222 (2022) 1511–1521.
- [90] C. He, H. Mou, W. Hou, W. Chen, T. Ao, Drought-resistant and water-retaining tobermorite/starch composite hydrogel for the remediation of cadmium-contaminated soil, *Int. J. Biol. Macromol.* 255 (2024) 127534.
- [91] H.-Y. Niu, J.-C. Li, J.-S. Li, C. Yi, C.-G. Niu, Preparation, properties and applications of porous hydrogels containing thiol groups for heavy metal removal, *J. Environ. Chem. Eng.* 11 (2023) 110983.
- [92] N. Rahman, A. Raheem, Adsorption of Cd (II) ions on magnetic graphene oxide/cellulose modified with β -cyclodextrin: analytical interpretation via statistical physics modeling and fractal like kinetic approach, *Environ. Res.* 243 (2024) 117868.
- [93] D. Xu, B. Zhao, Q. Luo, X. Du, X. Hao, Z. Liu, Acid promoted activity of UiO-66 as an efficient adsorbent for boron removal from aqueous solution, *Sep. Purif. Technol.* 317 (2023) 123855.
- [94] Z. Lin, F. Li, X. Liu, J. Su, Preparation of corn starch/acrylic acid/itaconic acid ion exchange hydrogel and its adsorption properties for copper and lead ions in wastewater, *Colloids Surf. A Physicochem. Eng. Asp.* 671 (2023) 131668.
- [95] H. Wang, S. Fang, M. Zuo, Z. Li, X. Yu, X. Tang, et al., Removal of copper ions by cellulose nanocrystal-based hydrogel and reduced adsorbents for its catalytic properties, *Cellulose* 29 (2022) 4525–4537.
- [96] Q. Zheng, Q. Li, Y. Tao, J. Gong, J. Shi, Y. Yan, et al., Efficient removal of copper and silver ions in electroplating wastewater by magnetic-MOF-based hydrogel and a reuse case for photocatalytic application, *Chemosphere* 340 (2023) 139885.
- [97] M. Dai, Y. Zhang, L. Zhang, Y. Tian, G. Liu, J. Zhao, et al., Multipurpose polysaccharide-based composite hydrogel with magnetic and thermoresponsive properties for phosphorus and enhanced copper (II) removal, *Compos. A: Appl. Sci. Manuf.* 157 (2022) 106916.
- [98] W. Ding, H. Sun, X. Li, Y. Li, H. Jia, Y. Luo, et al., Environmental applications of lignin-based hydrogels for Cu remediation in water and soil: adsorption mechanisms and passivation effects, *Environ. Res.* 118442 (2024).
- [99] P. Meetam, K. Phonlakan, S. Nijpanich, S. Budsombat, Chitosan-grafted hydrogels for heavy metal ion adsorption and catalytic reduction of nitroaromatic pollutants and dyes, *Int. J. Biol. Macromol.* 255 (2024) 128261.
- [100] C.B. Godiya, X. Cheng, D. Li, Z. Chen, X. Lu, Carboxymethyl cellulose/polyacrylamide composite hydrogel for cascaded treatment/reuse of heavy metal ions in wastewater, *J. Hazard. Mater.* 364 (2019) 28–38.
- [101] V.B. Lunardi, S.P. Santoso, A.E. Angkawijaya, K.-C. Cheng, P.L. Tran-Nguyen, A. W. Go, et al., Synthesis of cellulose hydrogel by utilizing agricultural waste and zeolite for adsorption of copper metal ions, *Ind. Crop. Prod.* 210 (2024) 118179.
- [102] X.-F. Sun, Y. Hao, Y. Cao, Q. Zeng, Superadsorbent hydrogel based on lignin and montmorillonite for Cu (II) ions removal from aqueous solution, *Int. J. Biol. Macromol.* 127 (2019) 511–519.
- [103] X. Chen, Z. Song, B. Yuan, X. Li, S. Li, T.T. Nguyen, et al., Fluorescent carbon dots crosslinked cellulose nanofibril/chitosan interpenetrating hydrogel system for sensitive detection and efficient adsorption of Cu (II) and Cr (VI), *Chem. Eng. J.* 430 (2022) 133154.
- [104] H.S. Mohamed, N. Soliman, D.A. Abdelrheem, A.A. Ramadan, A.H. Elghandour, S. A. Ahmed, Adsorption of Cd²⁺ and Cr³⁺ ions from aqueous solutions by using residue of *Padina gymnospora* waste as promising low-cost adsorbent, *Heliyon* 5 (2019) e01287.
- [105] L. Huang, S. Yuan, L. Lv, G. Tan, B. Liang, S. Pehkonen, Poly (methacrylic acid)-grafted chitosan microspheres via surface-initiated ATRP for enhanced removal of Cd (II) ions from aqueous solution, *J. Colloid Interface Sci.* 405 (2013) 171–182.
- [106] M. Aliabadi, M. Irani, J. Ismaeili, S. Najafzadeh, Design and evaluation of chitosan/hydroxyapatite composite nanofiber membrane for the removal of heavy metal ions from aqueous solution, *J. Taiwan Inst. Chem. Eng.* 45 (2014) 518–526.
- [107] G.Z. Kyzas, P.I. Siafaka, D.A. Lambropoulou, N.K. Lazaridis, D.N. Bikariaris, Poly (itaconic acid)-grafted chitosan adsorbents with different cross-linking for Pb (II) and Cd (II) uptake, *Langmuir* 30 (2014) 120–131.
- [108] S. Jamshidifar, S. Koushkbaghi, S. Hosseini, S. Rezaei, A. Karamipour, M. Irani, Incorporation of UiO-66-NH₂ MOF into the PAN/chitosan nanofibers for adsorption and membrane filtration of Pb (II), Cd (II) and Cr (VI) ions from aqueous solutions, *J. Hazard. Mater.* 368 (2019) 10–20.
- [109] M. Huang, H. Tu, J. Chen, R. Liu, Z. Liang, L. Jiang, et al., Chitosan-rectorite nanospheres embedded aminated polyacrylonitrile nanofibers via shoulder-to-shoulder electrospraying for enhanced heavy metal removal, *Appl. Surf. Sci.* 437 (2018) 294–303.
- [110] W. Chouyyok, Y. Shin, J. Davidson, W.D. Samuels, N.H. LaFemina, R.D. Rutledge, et al., Selective removal of copper (II) from natural waters by nanoporous sorbents functionalized with chelating diamines, *Environ. Sci. Technol.* 44 (2010) 6390–6395.
- [111] Y. Zhang, Z. Wei, M. Li, X. Wu, W. Wang, Preparation and modification of mullite whiskers/cordierite porous ceramics for Cu²⁺ adsorption and removing, *ACS Omega* 5 (2020) 15691–15701.
- [112] N. Jiang, Y. Xu, Y. Dai, W. Luo, L. Dai, Polyaniline nanofibers assembled on alginate microsphere for Cu²⁺ and Pb²⁺ uptake, *J. Hazard. Mater.* 215 (2012) 17–24.
- [113] L. Pan, Z. Wang, Q. Yang, R. Huang, Efficient removal of lead, copper and cadmium ions from water by a porous calcium alginate/graphene oxide composite aerogel, *Nanomaterials* 8 (2018) 957.
- [114] F. Qin, Z. Fang, J. Zhou, C. Sun, K. Chen, Z. Ding, et al., Efficient removal of Cu²⁺ in water by carboxymethylated cellulose nanofibrils: performance and mechanism, *Biomacromolecules* 20 (2019) 4466–4475.